Main Manuscript for

Constraining carbon loss from rivers following terrestrial enhanced rock weathering

Shuang Zhang[a,1], Christopher T. Reinhard[b], Shaoda Liu[c], Yoshiki Kanzaki[b], Noah J. Planavsky[d,e]

[a]Department of Oceanography, Texas A&M University, College Station, TX, USA
[b]School of Earth and Atmospheric Sciences, Georgia Institute of Technology, Atlanta, GA, USA
[c]School of Environment, Beijing Normal University, Beijing, China
[d]Department of Earth and Planetary Sciences, Yale University, New Haven, CT, USA
[e]Yale Center for Natural Carbon Capture, Yale University, New Haven, CT, USA

***Corresponding author**: Shuang Zhang
Email: shuang-zhang@tamu.edu

Author Contributions: S.Z., N.J.P., and C.T.R. designed research; S.Z. performed research; S.L. provided the river pCO_2 data; S.Z. analyzed data and contributed new modeling tools; S.Z., N.J.P., and C.T.R. wrote the paper, with contributions from S.L. and Y.K.

Competing Interest Statement: The authors declare no competing interest.

Classification: Physical Sciences (Major); Earth, Atmospheric, and Planetary Sciences (Minor)

Keywords: carbon dioxide removal; enhanced rock weathering; river degassing; carbon cycle; climate mitigation

This PDF file includes:
Main Text
Figures 1 to 3

Abstract

Enhanced rock weathering (EW) has garnered increasing interest as a promising technique for durable carbon dioxide removal, with a range of potential co-benefits including increased soil pH and nutrient release. However, the impacts of EW on river chemistry and the potential loss of initially captured CO_2 during river transport remain poorly constrained. The current lack of tools for robustly predicting the effect of riverine degassing on the EW life cycle undermines the use of this practice as a carbon mitigation strategy. Here, we present results from a first-of-its-kind dynamic river network model designed to quantify the impact of EW on river carbonate chemistry in North American watersheds. We map key water quality parameters across the river network of North America using machine learning, and use a dynamic river network model to simulate changes in river carbonate chemistry and carbon degassing during EW. Our model predicts low carbon loss (<5%) from river networks and limited changes to carbonate mineral saturation states for many of the river pathways explored here. However, there are some instances in which carbon degassing is significantly higher (>15%) and it is possible to induce large changes in carbonate saturation states, indicating that riverine carbon storage and the impacts of EW on river chemistry must be evaluated in a deployment-specific context. Although there remains uncertainty in the impact of EW on stream/river chemistry, our approach represents a step forward in the development of tools for quantifying the impacts of carbon cycling in downstream catchments on the overall EW lifecycle.

Significance Statement

Enhanced rock weathering (EW) has emerged as a promising long-term carbon dioxide removal (CDR) method with potential soil and crop co-benefits. However, its impact on river chemistry and the potential loss of captured CO_2 during river transport is unclear. We have developed a dynamic river network model to evaluate EW's effects on North American watersheds. Following EW application to a preliminary example set of locations, many rivers show low carbon loss and limited carbonate saturation state change. However, regional variation exists, emphasizing the need for deployment-specific evaluation and further development of process-based models of stream/river carbon cycling. This study provides a step forward in the development of tools for quantifying the impact of EW on river systems, supporting the potential for large-scale EW, and informing CDR strategy decisions and carbon markets.

Main Text

Introduction

There is growing recognition of the need for durable (long-duration) carbon dioxide removal (CDR) to meet climate targets in the coming century (1–3). Terrestrial enhanced rock weathering (EW) — the intentional application of crushed alkaline (carbonate or silicate) rock to soil to drive fixation of atmospheric CO_2 as dissolved bicarbonate (HCO_3^-) — has been suggested to offer a scalable, relatively low cost form of CDR with durability on thousand-year timescales (4–8). The potential magnitude of carbon removal through EW, though still poorly defined, may rival or surpass terrestrial ecosystem sequestration (e.g., via afforestation or soil organic carbon storage)

and is potentially >5 gigatons of CO_2 ($GtCO_2$; 10^9 tons) per year (5, 9–11). Because EW uses existing technology and infrastructure, it is ready to deploy and has potential for achieving relatively rapid scale alongside other efforts to help meet net-zero greenhouse gas emission goals. EW's potential for widespread adoption is further enhanced by a number of possible co-benefits, including enhancing crop growth via an increase in soil pH and improved availability and uptake of macro and micronutrients, reducing CO_2 emissions associated with traditional fertilizer production, and possible mitigation of soil emissions of nitrous oxide (e.g., 12–14).

Despite the potential of EW as an effective CDR strategy, there are still significant uncertainties that prevent generation of robust carbon removal from this practice, including the lack of a framework to track the downstream fate of carbon captured at the site of weathering. Foremost, there is no existing framework for tracking the dynamics of solute transport and storage through river networks following EW deployment. Although recent work has explored the first-order response of carbonate mineral saturation in river systems and its implications for carbon leakage (11, 15, 16), it is likely that the riverine carbon and solute transport following EW deployment will be impacted by CO_2 gas exchange between the river and the atmosphere upon mixing of multiple reach-scale river segments with varying dissolved inorganic carbon (DIC) and alkalinity (ALK) content (17). Integrated over the catchment scale, this process has the potential to significantly impact the overall efficacy of EW in sequestering atmospheric CO_2. In addition, existing work has focused on individual and disconnected rivers or watersheds, and there is no existing framework for tracking EW solute fluxes across catchment scales that incorporates river network topology and reach-scale interconnections in a time-dependent manner.

Here, we develop a dynamic river network (DRN) model that is designed to track the transport and transformation of EW products through river systems from the reach to the continent scale. The DRN model builds upon existing river network delineation (e.g., 18, 19) and uses comprehensive data sources, machine learning methods, and reaction-transport principles to achieve predictions of key river hydrochemistry parameters following EW deployment. We focus here on tracking the impacts of EW on the North American rivers, but once fully developed and validated the framework can in principle be applied to any region of interest given rapid advances in the global reach of digital elevation models (DEMs) and river network data.

Building the DRN model framework

There are four key steps in constructing the DRN model (Fig. S1). First, we compile key water quality parameters from existing river stations across the contiguous United States (CONUS). Second, we build the river network topology by connecting river segments that either flow through the CONUS or receive water from rivers flowing through the CONUS. We define this set of river segments as our North American river network. Third, we use machine learning to predict the key water quality parameters for the whole North American river network based on the discrete water quality dataset and their corresponding watershed properties as a training set. Lastly, we construct the DRN model based on the predicted key water quality parameters, river hydrology/geomorphology, and reconstructed pCO_2 values from prior analysis. Once configured, this DRN model can then be used to dynamically track river responses to introduction of solutes from EW.

To establish the baseline chemistry (before implementing EW) of North American rivers, we assimilate hydrogeochemistry data for the CONUS from the United States Geological Survey (USGS) (20), including comprehensive data for ALK, Ca, pH, salinity, and water temperature (Fig. S2). Based on these parameters, the monthly baseline carbonate saturation state values (Ω) for the CONUS rivers can be calculated (Fig. S3). To interpolate the spatially disconnected hydrogeochemistry data into a seamless reach-scale river network across North America, we first extract North American river network and topology data from the Global Reach-scale A priori Discharge Estimates for SWOT (GRADES) river network (18). This extensive network offers detailed global river reach topology and morphology (such as channel slope), along with daily discharge estimates at the reach scale over a 35-year period. Based on GRADES, we determine the monthly river surface area and volume (Fig. S4) of each river segment (*Materials and Methods*). We then employ a random forest (RF) machine learning algorithm, which can predict key water quality parameters (ALK, Ca, salinity, and water temperature) throughout the North American river network from compiled North American watershed parameters (i.e., climate-hydrology parameters, lithology, land cover, geomorphology, and soil properties) (Fig. S5-S8). We subsequently merge the water quality parameters predicted by the RF model, together with river discharge, surface area, and volume, with the river pCO_2 values reconstructed in prior work by ref. (19) to form a single consolidated dataset. This dataset serves two purposes: first, to compute the background monthly carbonate system (for example, DIC and carbonate saturation state) and CO_2 degassing flux for each river segment across North America; and second, to be utilized subsequently in the DRN model.

After consolidating the river network data, we proceed to construct a system of ordinary differential equations (ODEs) (Eq. 1–4) tracking the carbon budget in each discrete river segment. This ODE system (the DRN model) treats each river segment as a single reservoir and explicitly tracks tracer fluxes (DIC, ALK, Ca, and salinity) through and between reservoirs following EW implementation:

$$\frac{dDIC}{dt} = F_{up\_DIC} - F_{down\_DIC} - F_{degass\_DIC} + F_{other\_DIC} + F_{EW\_DIC} \quad (1)$$

$$\frac{dALK}{dt} = F_{up\_ALK} - F_{down\_ALK} + F_{other\_ALK} + F_{EW\_ALK} \quad (2)$$

$$\frac{dCa}{dt} = F_{up\_Ca} - F_{down\_Ca} + F_{other\_Ca} + F_{EW\_Ca} \quad (3)$$

$$\frac{dSalinity}{dt} = F_{up\_Salinity} - F_{down\_Salinity} + F_{other\_Salinity} + F_{EW\_Salinity} \quad (4)$$

where F_{up} terms trace the flux from the joining upstream reach, F_{down} terms trace the flux flowing out of the current reach, F_{other} terms represent "residual" partitioning fluxes within each reach (implicitly including carbonate precipitation and net carbon metabolism), which can be solved inversely using a mass balance approach (*Materials and Methods*), and F_{EW} traces the solute flux derived from EW. The DIC mass balance contains an additional term — F_{degass} — which

represents the carbon exchange flux between a given river reach and the atmosphere and can be calculated using the following equation.

$$fCO_2 = k \cdot ([CO_2]_r - [CO_2]_a) \quad (5)$$

where $[CO_2]_r$ represents the CO_2 concentration in river, $[CO_2]_a$ represents the CO_2 concentration in river that is in equilibrium with the atmosphere, and k represents the gas transfer velocity at the water–air interface. The *k* value for each river segment is quantified based on its flow regime (low- vs. high-energy streams) using channel slope, flow velocity, and water temperature as parameters (21–23) (*Materials and Methods*).

The ODE system (Eq. 1–4) allows us to track dynamic changes to river chemistry in any downstream reach in response to the input of EW products into any river segment. Coupling the dynamic evolution of DIC, ALK, Ca, and salinity with other river properties (e.g., water temperature, surface area) allows us to solve the complete system of carbonate species, the carbonate saturation state, and carbon degassing flux for each river reach through time. Subsequently, the cumulative carbon leakage with time for each river flow path can be calculated. (*Materials and Methods*).

Tracking river responses to EW using the DRN model

Prior to deploying our DRN model to simulate the river responses to EW, we first assess the model's ability to capture background monthly fluctuations in river chemistry. As a case study, we use the longest Mississippi flow path to compare model predictions with actual monthly river signals for randomly chosen river segments. Encompassing a broad spectrum of spatial scales, diverse lithological characteristics, and varied climatic conditions, the Mississippi river and its watershed function as a multifaceted natural laboratory. Coupled with its extreme river data density (24), this flow path provides a useful baseline for validating the performance of our DRN model. We run the model from day 0 for each river segment along the Mississippi flow path for two years without any EW input, utilizing a time step of 0.1 day, then compare the modeled DIC and ALK time series with the background monthly DIC and ALK values from empirical data.

We next introduce EW solutes into a randomly selected river segment in North America and run our DRN model to track the downstream river chemistry change and carbon degassing (e.g., carbonate saturation state and carbon degassing flux). The model outcome also enables us to monitor integrated carbon leakage during the transport of EW solutes along the entire flow path. In our simulation, basalt serves as the EW feedstock. Owing to its fast reaction rate, relatively high Mg and Ca content, and widespread availability, basalt is often chosen as the primary rock type for EW applications (5, 25). After basalt is spread to the watershed of river segment, we assume it dissolves congruently and all dissolved solutes enter the selected river segment. The dissolution rate is set as 1 ton of basalt per hectare per year in our baseline scenario, a reasonable assumption that is comparable to previous modeling and field studies (5, 9, 26). We then multiply this assumed dissolution rate by the watershed area of the selected river segment to determine the total annual input of basalt solutes into the river segment. From this, the daily input of basalt solute into the river segment is derived and fed into our DRN model. Notably, applying this dissolution rate to the global land surface would result in a global basalt dissolution flux of 15 Gt/yr. Although this

global enhanced basalt dissolution rate falls within the range of recent estimates of the global river capacity to transport dissolved from basalt weathering without inducing carbonate precipitation (11), we do not advocate for the likelihood of any particular scenario here. Instead, this value is only meant to illustrate a scenario of relatively large-scale EW deployment. We also emphasize here that the basalt dissolution rate adopted in this study is not determined by mechanistic reaction kinetics. However, the DRN model is designed to be flexibly coupled with solute fluxes derived from field measurements or reaction-transport models of soil biogeochemistry.

After setting up the EW input to the selected river segment, we run our DRN model over 2 years to determine the changes in river chemistry and carbon leakage for the whole flow path through time. To examine the regional differences in carbon leakage due to incoming EW solutes, we repeated the model simulation with 100 different random river segments. These 100 different river segments are sampled with equal probability from all North American river segments and broadly cover the climatic and hydrogeochemical heterogeneity of the North American continent. For each river segment, we apply basalt to its corresponding watershed and set the basalt dissolution rate at 1 ton per hectare per year in the baseline scenario. This rate is then multiplied by the watershed area of the river segment (Fig. S9A) to calculate the total annual input of basalt solutes into the river segment (Fig. S9B). Our DRN model is run over 2 years for each segment to assess the river chemistry change and carbon leakage through time. In total, we conduct 100 DRN model runs over the North American river network.

Sensitivity tests of the DRN model

We conduct 10 sensitivity tests of the DRN model to assess the impact of river discharge and gas transfer velocity (k) values on the simulated carbon leakage rate across the river network. First, we randomly sample the monthly discharge values for each river segment 10 times, adhering to a normal distribution based on the mean and standard deviation provided by GRADES. Concurrently, k values are recalculated for each set of resampled discharge values (see *Materials and Method* for the relationship between k and discharge). We then reconstruct the DRN model and perturb it with EW at each of the selected 100 sites, employing each set of resampled discharge values and the recalculated k values. The carbon leakage from these 10 iterations is quantified and compared to the DRN model output for the baseline scenario. We also explore two additional basalt dissolution scenarios — targeting 0.5 ton of basalt dissolved per hectare per year and 1.5 ton of basalt dissolved per hectare per year, respectively — to test model sensitivity to variations in the magnitude of EW. We define the 0.5 ton as the low scenario and the 1.5 ton as the high scenario.

Results and Discussion

River chemistry and carbon degassing in North America

Our compiled river chemistry data provide broad spatial coverage across the CONUS, comprehensively representing its geographical diversity (Fig. S3). The prior distribution of carbonate saturation state values (Ω) in U.S. rivers is strongly right-skewed (Fig. S3). In January, 84% of the Ω values are below 5, and 96% are below 10; in July, these numbers are 76% and 90%, respectively. The slightly higher Ω values in the summer reflect the aggregate impacts of seasonal shifts in river chemistry and hydroclimatic parameters. In particular, increased temperature

(leading to lower CO_2 solubility), accelerated background chemical weathering in watersheds (and thus greater alkalinity flux into rivers), and human activities (intensified agricultural practices and wastewater discharge) all impact seasonal shifts in Ω, and these will vary based on the specific geography and ecology of each river segment. Across all months, 81% of the Ω values are below 5, and 93% are below 10.

The RF model performs reasonably well at predicting key water quality properties at the reach scale from assimilated USGS gauging stations (Fig. S5-S8). For all target variables (i.e., ALK, Ca, salinity, and water temperature), the trained model produces $R^2 > 0.75$ when applied to the test data, suggesting that our framework is capable of explaining more than 75% of the inherent variability in the target variables of unobserved river stations. By utilizing the consolidated dataset that includes river ALK, Ca, salinity, and water temperature predicted by the RF model, along with the river channel slope, discharge, surface area, volume, and pCO_2 values, we can solve the whole carbonate system (for example, DIC and CO_3^{2-}) for each river segment and reconstruct the monthly carbon degassing flux and carbonate saturation states across the North American river network (Fig. 1). The calculated carbon degassing flux reveals a considerable degree of spatial heterogeneity and strong temporal fluctuations (Fig. 1A,C). For example, the degassing flux varies spatially among segments from -0.02 to 19 gC m^{-2} d^{-1} and between 5 x 10^{-7} to 31 gC m^{-2} d^{-1} for January and July, respectively. The degassing flux observed in July generally exceeds that in January, consistent with ref. (19), which can be linked to higher river pCO_2 levels and elevated gas transfer velocity during summertime, as well as seasonal variations in watershed hydrology. Similarly, the reconstructed Ω values across North America exhibit substantial spatial and temporal variation. Values in July typically surpass those in January (Fig. 1B,D). Overall, the distribution of Ω values is right skewed, with the majority falling below 10 — comprising 84% in January and 80% in July. These low background Ω values suggest *a priori* that the North America river network possesses a significant capacity to assimilate EW solutes without inducing significant net carbonate precipitation, as carbonate precipitation in river waters tends to be negligible when Ω is below ~10, and in many cases insubstantial carbonate precipitation is observed in systems with Ω values well above 10 (16, 27–29).

Model performance in reconstructing background river chemistry and carbon degassing

We observe close correspondence between DRN model predictions and background monthly dissolved ALK and DIC (which in turn constrain the carbonate system) for the 1st, 200th, 400th, 600th, and 771st river segments along the longest Mississippi flow path (Fig. S10). Specifically, the monthly averaged relative error for DIC ranges from 0.012% to 0.14% for our benchmark segments. For ALK, the range is also 0.012% to 0.14% for the same segments. This agreement indicates the F_{other} terms in Eq. 1-4 are solved accurately and our DRN model could reconstruct the background river chemistry before any ERW input. Comparison of predicted monthly carbon degassing with observation-based estimates (e.g., calculated gas exchange fluxes based on discrete solute measurements) for river segments in central Connecticut and New Hampshire (30, 31) yields an $R^2 = 0.7$ (Fig. S11). Although our predicted values and the observation-based estimates are generally in agreement, measurement-based estimates still bear large uncertainty (as evidenced by the big error bar in Fig. S11), making the comparison with model predictions challenging. Comprehensive empirical constraints on stream/river CO_2 gas exchange for validation of this and other predictive models of inland water CO_2 cycling is an obvious future research topic.

River leakage following EW and the controlling factors

With EW applied at each of the 100 random sites (Fig. 2A) individually over 2 years, the DRN model tracks the downstream responses for each flow path through time. As expected, the longer flow paths tend to exhibit a higher predicted total carbon degassing flux (Fig. S12). However, cumulative carbon leakage, defined as the ratio of additional carbon degassed from the river to the atmosphere compared with carbon degassed in the background state relative to the total DIC added to the headwater following the EW application (*Materials and Methods*), is generally below 5% for the baseline scenario. The cumulative leakage experiences a steep increase at the beginning of the model simulation and then remains relatively unchanged throughout the simulation period (Fig. 2B). After applying EW for durations of 6, 12, 18, and 24 months, the percentages of flow paths with cumulative carbon leakage rates < 5% are 91%, 99%, 93%, and 94%, respectively (Fig. 2C). Two flow paths out of the 100 simulated here exhibit significantly higher leakage rates. Specifically, path 1 experiences carbon leakage approaching 20% and path 2 exceeds 5% carbon leakage for the majority of the model simulation period. The maximum cumulative leakage rate for the baseline scenario stands at 20.3%. The additional 10 sensitivity tests associated with this scenario reveal carbon leakage patterns closely aligned with those observed in the initial baseline output (Fig. S13). Across the 100 flow paths, the maximum cumulative carbon degassing fluctuates between approximately 20.2% and 23.6% for these tests, with most flow paths showing low carbon leakage throughout the simulation period. After 24 months, 93% of river flow paths exhibit carbon leakage below 5% in the 10 sensitivity tests. Similarly, the low and high scenarios demonstrate carbon leakage patterns that are consistent with the baseline scenario (Fig. S14). We also observe that carbon leakage is smaller in the low scenario compared to the baseline scenario, while carbon leakage is higher in the high scenario compared to the baseline scenario.

The median carbonate saturation state (Ω) for each of the flow paths in the baseline scenario remains low and is largely unaltered after EW application when compared with the background state at each duration (Fig. 2D). However, much like the seasonal fluctuations observed in the background data, the carbonate saturation state is higher overall during summer months (after 6 or 18 months) than winter months (after 12 or 24 months) (Fig. 2D), which is potentially attributable to increased temperature, accelerated background chemical weathering in watersheds, and human activities. After the continuous application of EW for either 6 or 18 months, approximately 66% of the river flow paths displayed median Ω values less than 10, and approximately 92% displayed Ω values less than 15. In contrast, following 12 or 24 months of continuous EW application, around 86% of all river segments exhibited median Ω values below 10, and approximately 97% displayed Ω values less than 15. Nonetheless, some flow paths showed extremely high Ω values ($\Omega > 100$), particularly in the first sediments downstream of EW deployment (Fig. S15), indicating a clear need for a better understanding of calcium carbonate formation and recycling in bedload sediments under transient extremes in carbonate saturation state.

Our study indicates a strong positive association between the median cumulative carbon leakage rates and median carbonate saturation states across flow paths for sustained durations encompassing 6, 12, 18, and 24 months (Fig. S16A). This relationship predominantly originates from the strong positive correlation between alkalinity and carbonate saturation states in the river (Fig. S16B), and the impact of alkalinity on carbon degassing. We argue that the EW DIC:ALK ratio and their absolute amounts, coupled with the unique hydrological attributes of the river

segments, control the dynamics of carbon leakage rates during EW implementation. Implementing an EW input with a DIC:ALK ratio of 1, as adopted by this study (*Materials and Methods*), will lead to an increase in the pCO_2 value in the river, as dictated by the thermodynamic relations involving DIC, ALK, and the equilibrium fluid pCO_2 (Fig. S17). Consequently, the river will shift towards more carbon degassing, resulting in a leakage of carbon from the river system (Fig. 2B). Furthermore, larger input of DIC and ALK will result in commensurately greater elevation in riverine pCO_2 (Fig. S17), fostering increased degassing and, consequently, enhanced carbon leakage. The elevated leakage rates exhibited by the two flow paths discussed above (Fig. 2B) can be explained by the temporal patterns of alkalinity in those river segments (Fig. S18A), which are in turn governed by the ratio of the alkalinity flux to the flow path volume over time (Fig. S18B). Similarly, the varying carbon leakage rates across the three basalt dissolution scenarios (Fig. S14) can also be attributed to differences in the alkalinity fluxes into the river segments, with higher leakage rates associated with higher alkalinity flux.

Being the recipient of basalt dissolution products, the first river segment is poised to respond more swiftly to EW applications, making it an ideal focal point for examining the interactions between EW applications and river responses. The fluctuation in a river segment's alkalinity can be modulated by various factors including the alkalinity input flux and the river flow dynamics. Not surprisingly, after alkalinity injection, we observe a positive correlation ($r = 0.58$) between the alkalinity input flux and the shift in alkalinity, relative to the concurrent background state, in the first segment (Fig. S19A). At the same time, we observe a strong negative correlation ($r = -0.76$) between the segment volume and the shift in alkalinity (Fig. S19B). Theoretically, segments with either a smaller volume or a higher influx of basalt dissolution products from EW will exhibit a more pronounced response due to a more dramatic increase in the ALK (as well as DIC) concentration. Here, a surge in alkalinity in the first segment is directly associated with elevated leakage rates after day 1 ($r = 0.81$; Fig. S20). This rapid response of the first segment to the incoming EW solutes also accounts for the sharp increase in carbon leakage rate observed at the onset of our model simulation (Fig. 2B). In summary, our findings suggest that carbon leakage is predominantly controlled by both EW input fluxes and the hydrological conditions of individual river segments, with seasonal variations in flow dynamics playing a significant role in determining fluctuation in carbon leakage rate across systems.

Spatial heterogeneity of river leakage and river chemistry following EW

Following the HydroSHEDS watershed delineation scheme (32), we subdivide the river flow paths explored here into seven watershed regions across North America—Middle, North, Northeast, Northwest, South, Southeast, and Southwest (Fig. 3). This allows us to quantify the variations in cumulative carbon leakage rate and carbonate saturation state across these regions. The median cumulative carbon leakage rate of the flow paths after 24 months of EW application in our randomized deployment scheme increases in the following order: Southeast (0.6%), Northeast (1.4%), North (1.7%), Northwest (2.5%), Middle (2.8%), South (4.7%), and Southwest (4.9%) (Fig. 3A). The median carbonate saturation state of the flow paths increases in a similar order: Southeast (0.02), Northeast (0.9), Northwest (1.9), North (3.6), Middle (4.0), Southwest (9.1), and South (10.3) (Fig. 3B). Our study finds a positive correlation between median cumulative carbon leakage rates and median carbonate saturation states in various regions (Fig. S21). This finding aligns with the observed positive correlation between carbon leakage rates and carbonate saturation states across individual flow paths (Fig. S16A), supporting the strategic selection of

river watersheds with low initial carbonate saturation for real-world EW application. Such rivers not only accommodate EW products more effectively but also exhibit lower carbon leakage, maximizing EW's net impact on atmospheric CO_2 sequestration. The distribution of cumulative carbon leakage rates is irregular both within each region and among different regions (Fig. 3C), implying significant heterogeneity in river hydrochemistry and watershed properties. Notably, the southwest region, which displays the highest median carbon leakage rate, also encompasses the two flow paths that exhibit the highest carbon leakage rates among the 100 flow paths studied here (Fig. 2B). This phenomenon is likely to be attributed to the pronounced evapotranspiration and dry conditions in the southwest, which lead to diminished river flow and storage, thereby amplifying the impact of EW on solute chemistry and facilitating higher leakage rates. Spatial heterogeneity is also evident in the carbonate saturation state of all river segments, both within each region and across different regions (Fig. 3D). This strong heterogeneity in carbonate saturation state and river leakage rate indicates a need to use deployment-specific information for any EW project attempting to create carbon offsets, as specific deployment regions and flow paths can potentially be characterized by much larger CO_2 degassing than the aggregate statistics would imply.

Implications for evaluating river/stream CO_2 leakage in EW deployments

In aggregate, our results suggest limited carbon leakage during riverine carbon transport and relatively low carbonate saturation state in the river network during EW application. Nonetheless, spatial heterogeneity is evident and non-trivial carbon leakage in rivers is ubiquitous, and in some cases can be large, such that any compensatory claims on CO_2 emissions made based on the generation of EW-based carbon credits need to explicitly take this carbon loss into account or measure it empirically. Although the current DRN framework does not explicitly account for changes in carbonate precipitation resulting from the addition of EW products to river systems, our simulations show generally very small changes in the carbonate saturation state of most rivers despite very high assumed total EW solute fluxes. In addition, it is possible that carbonate formed at the reach scale will subsequently dissolve in bedload sediments due to extensive CO_2 production from aerobic respiration (33, 34). Nonetheless, more realistic deployment scenarios than that explored here — in particular situations in which one or multiple suppliers are operating at scale in a relatively small region — could potentially lead to dramatic changes in carbonate saturation states that lead to more carbonate precipitation than the background state. For example, our results clearly show that initial river segments downstream of EW solute release see much larger changes to carbonate saturation state (Fig. S15) than other segments (Fig. 2D) downstream. This provides additional rationale for assessing the impact of individual EW projects on surface waters in a deployment-specific context and the need for full data transparency in EW projects. Further, this work also strongly suggests that new frameworks to prevent the overuse of a common good—rivers—will need to be established.

By elucidating the riverine responses to EW, we can also more accurately define the boundary conditions for river fluxes to the ocean under various EW scenarios (35). Interestingly, as inferred from the thermodynamic relationships involving DIC, ALK, and equilibrium pCO_2 (Fig. S17), a river flow path experiencing increased carbon degassing during the transport of EW products will exhibit a lower DIC:ALK ratio in its final flux to the ocean. This, in turn, will mitigate the rise of pCO_2 levels in the seawater upon receiving the river flux, resulting in reduced carbon degassing from the seawater to the atmosphere (or possibly resulting in ingassing). In other words, our results imply that carbon leakage from river systems and subsequent loss from the surface ocean (7) are

not additive, and that carbon loss during riverine transport will decrease net carbon loss to degassing in the surface ocean. The exception to this dynamic would be large-scale cation removal during transport to the coastal ocean through secondary carbonate or clay formation, which remains an important topic for future research. In any case, our model sets the stage for future modeling efforts aimed at understanding the ocean's response to EW products transported by rivers in a regional, deployment-specific context.

The presented DRN model framework is meant to be a step forward in the development of tools that can provide a more realistic and comprehensive assessment of the impact of EW. However, there are still uncertainties in our ability to accurately predict river/stream degassing of CO_2 across a range of relevant scenarios—and a need to further validate this model framework with large-scale EW trials. Our analysis should not be taken as an indication that a relatively minor discount to field CDR rates can be uniformly applied to compensate for the effects of EW on rivers regardless of deployment strategy or location. Future studies should focus on refining the DRN model by incorporating the dynamics of carbonate precipitation in response to the addition of EW products, as stressed by ref. (15). Additionally, the model should be enhanced by integrating more comprehensive carbon cycling processes, such as metabolic activity (36–38). Lastly, coupling the DRN framework with mechanistic models of upstream processes, such as feedstock dissolution in soils and cation storage and transport in the lower vadose zone, will be required to provide more realistic predictions of the impacts of EW on river chemistry and catchment-scale degassing.

Conclusion

We introduce a dynamic river network model designed to explore the impacts of EW on river systems across scales. In aggregate, results from a quasi-randomized EW deployment scenario yielded relatively minor shifts to carbonate mineral saturation states in most downstream river segments, but the potential for high degree of supersaturation locally. Overall carbon leakage, from carbonic acid system re-equilibration, was found to be generally below 5% throughout the two-year simulation period across North American watersheds. However, impacts will be region- and deployment-specific, and it will be important to validate these results with empirical observations and additional simulations with more realistic deployment architectures. Nonetheless, this work represents a step forward in understanding and predicting the carbon degassing of river networks and the water chemistry impacts of EW. Moving forward, further development of open tools such as the DRN network presented here has the potential to inform policy decisions and be utilized in carbon marketplaces, highlighting the value of continuing to investigate, refine, and critically interrogate all aspects of the EW process.

Materials and Methods

River data compilation

We collect a suite of river chemical species and properties (ALK, Ca, salinity, pH, water temperature and discharge) through the CONUS from USGS (20). We select eleven different parameter codes for alkalinity (00418, 00421, 29801, 29802, 29803, 39036, 39086, 39087, 99431, 00410 and 90410), two parameter codes for calcium (00915 and 91051), three parameter codes for salinity (i.e., total dissolved solids) (70300, 70301 and 00515), three parameter codes for pH

(00400, 00403, and 00408), and one parameter code for temperature (00010) according to the USGS parameter coding system. To calculate flux-weighted species concentration, we further collect river discharge rates (parameter code 00060). For each of these parameters, we remove the samples that are not labeled as "Surface Water" from our river sample dataset. We further calculate the average value of each of the parameters for the samples that have the same "ActivityIdentifier". Outlier data, defined as values higher than the 99th percentile of each parameter, are removed. Sites with multiple measurements in a day are averaged on a daily basis for each parameter, after which all parameters are matched together based on the unique site number and sampling date. To maintain a high-quality monthly signal, we remove the sites that lack at least one data point for each month. After data filtering, the monthly value of each parameter for each river station is calculated by aggregating the samples by month, weighted by the discharge rate. We further remove the river sites that do not have drainage area recorded in the USGS database. This yields our final dataset for river chemistry, which contains 1995 river sites, and each site contains 12 monthly values for each property. The distribution of each river property can be found in Fig. S2. Complete monthly carbonate system (such as $[CO_3^{2-}]$) then could be solved from the monthly ALK, pH, salinity, and water temperature at each site using the *seacarb* package (39), considering the impact of both temperature and salinity. Subsequently, calcite saturation state (Ω) in the 1995 sites (Fig. S3) could be calculated based on solute chemistry, temperature, and salinity according to the following equation (11):

$$\Omega = \frac{[Ca^{2+}][CO_3^{2-}]}{K_{sp}} \quad (S1)$$

where K_{sp} represents the apparent solubility product for calcite corrected for site-specific temperature and salinity (40) and brackets denote concentration. Eq. S1 is also used in the DRN model to calculate the evolution of Ω values in each river segment. We only present calcite Ω values given the argonite, dolomite, and other carbonate minerals are unlikely to precipitate.

Building the river network in North America

We use the Global Reach-scale A priori Discharge Estimates for SWOT (GRADES) river network (18) to build the river topology in North America. GRADES provides a topology of global river reaches (close to 3 million individual ones), coupled with estimates of daily discharge at each reach scale, spanning across a substantial 35-year period. It has the length (L), watershed boundary, and connectivity to other segments for each river segment. We overlay the watersheds of GRADES on the CONUS and extract the ones that intersect with the CONUS. We then extract the final water outlets for all those watersheds and further extract all the river segments whose final outlets match those watershed outlets. Specifically, wherever we apply EW on the CONUS land surface, the downstream flow path is contained in this data set.

Based on the river connectivity, we delineate the whole downstream flow path starting from each river segment for the North America, which paves the way for us to feed into the EW solutes to any segment and to track the downstream response. The monthly width of the river segment is derived from ref. (19), estimated by integrating both the downstream hydraulic geometry (DHG) and at-a-station hydraulic geometry (AHG) relationships for width. With the segment length and monthly width, we calculate the monthly segment surface area (Fig. S4A,C). Following ref. (19),

the flow velocity for each segment is estimated from monthly discharge and a gauge-derived discharge-velocity (Q-V) relationship (i.e., $\ln V = 0.12 \ln Q - 1.06$) (41), which predicts reliable velocity over a broad range of river discharge (0.01 to 20,000 $m^3\ s^{-1}$). With monthly river discharge and flow velocity, we calculate the monthly cross section area (A) of each segment (i.e., A = Q/V) and further calculate the monthly volume of each segment (i.e., Volume = A * L) (Fig. xx)

Gas transfer velocity (k) is estimated from channel slope and flow velocity, which together correspond to the decaying dissipation energy (ε_D) along river networks and have been shown to be able to predict reasonable k over large spatial scales in various regions (23). We use a slope cutoff of 0.01 (19) to differentiate low- vs. high-energy alpine streams (21), and calculate the k value for these two types of streams separately.

For streams not affected by high bubble-mediated gas exchanges in steep terrains, k was estimated directly from channel slope and flow velocity (22):

$$k_{600} = 2841SV + 2.02 \ (S2)$$

where k_{600} is the gas transfer velocity at a common Schmidt number (Sc) of 600 (for CO_2, the Schmidt number at around 20 ℃), S is channel slope (m/m) and V is flow velocity (m/s). Specifically, channel slope is directly from the GRADES river networks. Flow velocity is derived by coupling monthly discharge from the GRADES dataset to a gauge-derived Q-V relationship as shown above.

For streams affected by high bubble-mediated gas exchanges in steep terrains, k was estimated using a reported power law relationship between k_{600} and the dissipation energy (ε_D, $m^2\ s^{-3}$) (21):

$$\ln(k_{600}) = 1.18 \ln(\varepsilon_D) + 6.43 \ (S3)$$
$$\varepsilon_D = gSV$$

where g is gravitational acceleration ($m\ s^{-2}$).

Finally, the following relationship is used to convert estimated k_{600} to gas transfer velocity (k) at specific temperatures for each month.

$$k_{in\ situ} = k_{600} \left(\frac{Sc_{CO_2}}{600}\right)^{-2/3} \ (S4)$$

where 600 is the Schmidt number of CO_2 in freshwater at 20 ℃. Sc_{CO_2} is the Schmidt number for CO_2 at specific temperatures in freshwater and can be calculated as:

$$Sc_{CO_2} = 1742 - 91.24T_w + 2.208T_w^2 - 0.0219T_w^3 \ (S5)$$

where water temperature (T_w in ℃) is estimated (along other key water quality parameters) from machine learning in this study.

Watershed property compilation

We compile a suite of watershed properties used to predict the water properties (Ca, ALK, salinity and water temperature) over North America. First, we delineate the total upstream watershed for each river segment based on the river topology and individual watershed for each segment. Second, for each delineated upstream watershed, we calculate the average value of watershed properties, including monthly temperature and precipitation (42), monthly runoff (43), monthly soil moisture (44), surface lithology (45), land cover (46), land erosion rate (47, 48), soil pH and organic carbon content (49), net primary productivity (50), and nitrification rate (51). Third, we match the collected river stations (from USGS) to the appropriate river segment. To achieve this, we search within a 20 km radius centered on each river station to find the nearest river segment. We ensured that this segment's total upstream watershed area is similar to the drainage area provided by the USGS, allowing for a difference of less than 50%. After snapping, we extract the watershed properties for each river station from the already compiled watershed properties over the whole North America river network. Finally, we merge the river chemistry at each river station with its corresponding watershed properties into a dataset that will be used to train a machine learning framework. The watershed properties over the whole river network in the North America will be fed into the trained machine learning framework to map the river properties over North America.

Mapping river properties over the North American river network using machine learning

We employ the Random Forest (RF) algorithm, a tree-based ensemble supervised machine learning technique that offers several advantages over other machine learning techniques, including low bias and moderate variance (52). RF is based on decision tree, which is a non-parametric supervised learning algorithm used for classification or regression. Decision tree captures non-linear relationships in the data and is robust to input outliers (53). However, decision trees can also be prone to overfitting (i.e., high variance), relatively low in predictive accuracy and does not yield optimal solutions. RF can be thought of an ensemble of many trees (called the bagging technique), and it reduces the high variance experienced by a single decision tree. Different than simple bagging, RF further decorrelates the trees by using a random set of predictor variables to divide the training data during each splitting. All these modifications contribute to the high predictive accuracy (low bias and moderate variance) of RF. The RF algorithm has been widely used in geoscience research (e.g., 52) and is particularly suitable for making predictions using high dimensional data with complex non-linear relationships, such as our dataset.

The construction of the RF model is conducted in R (55) using the "ranger" package (56). We build a regression domain, in which the monthly river Ca concentration, ALK, salinity, and temperature are the target variables and the potential factors (watershed properties) that influence those river parameters are the predictor variables. We split the whole data into a training dataset (75% of the data) and a test dataset (the remaining 25% of the data). The training set, as the name suggests, is used to train the model — allowing it to learn the relationship between the predictor variables and the target variable. The testing set, on the other hand, is employed to evaluate the performance of the model on unseen data, providing an estimate of how accurately the model would predict with new data. During the training process, we select 500 for num. trees (i.e., the number of sub-models) and 3 for min.node.size (i.e., the minimal size of the tree branch in each sub-model) as our model hyperparameters. After model training and testing, we retrain the model on the whole dataset. This

final model, trained on all available data, is considered to have optimized learning from the given dataset, and thus should offer the best possible performance when deployed to handle real-world data. We then feed the compiled watershed properties over the whole river network in North America into the final machine learning model to obtain the Ca, ALK, salinity and water temperature over the North America river network. These water properties are joined with previously modeled river pCO_2 values (19) to further quantify the background monthly carbonate system chemistry and carbon degassing flux for each river-reservoir segment (Fig. 1).

DRN model setup

The DRN model is designed to be able to quantify the dynamics in the carbonate system (carbon mixing, saturation state shifts, and carbon degassing) in each river segment downstream following the application of EW in any watershed. The core of the DRN model is the ODE system (Eq. 1-4). First, we need to make sure our DRN model could reconstruct the background river dynamics before running any EW simulation. Accordingly, the initial equations (Eq. 1–4) will be modified to:

$$\frac{dDIC}{dt} = F_{up\_DIC} - F_{down\_DIC} - F_{degass\_DIC} + F_{other\_DIC} \ (S6)$$

$$\frac{dALK}{dt} = F_{up\_ALK} - F_{down\_ALK} + F_{other\_ALK} \ (S7)$$

$$\frac{dCa}{dt} = F_{up\_Ca} - F_{down\_Ca} + F_{other\_Ca} \ (S8)$$

$$\frac{dSalinity}{dt} = F_{up\_Salinity} - F_{down\_Salinity} + F_{other\_Salinity} \ (S9)$$

As F_{up}, F_{degass}, and F_{down} can all be calculated directly from our synthesized river parameters, the key step to complete the whole ODE system is to inversely calculate the term F_{other}, which can be readily finished following the mass balance equation. Specifically, we interpolate the monthly signal of all river parameters (e.g., DIC, ALK, salinity, Ca, water temperature, river surface area, river volume, river discharge) to daily signal using the monotone Hermite spline method (57), which yields a much more smooth spline than the linear interpolation method. Then, we calculate the value of the derivative (e.g., $\frac{dDIC}{dt}$) as well as the F_{up}, F_{degass}, and F_{down} at each day and then solve F_{other} at each day for each tracer based on mass balance. Specifically, F_{other} at each day can be easily obtained by calculating the difference between $\frac{dDIC}{dt}$ and F_{up}+ F_{degass} + F_{down}. Finally, we build the function for F_{other} change with time, which will be further used in the forward ODE equations (both the background Eq. S6–S9, or EW Eq. 1–4). To test whether our DRN model could reconstruct the background river dynamics, we pick the longest flow path in North America (the Mississippi river) and ran our ODE system (Eq. S6-S9) for this flow path from day 0 for 2 years. To run the ODE, we utilized the “vode” ode solver in the “deSolve” package (58). The "vode" solver, also known as the Variable-coefficient Ordinary Differential Equation solver, is particularly effective in handling "stiff" ODE problems. To further enhance the model

accuracy, we decreased the relative error tolerance from the default 1e-6 to 1e-7. The time step for saving the ODE output was set to be 0.1 day.

Tracking river responses to EW using the DRN model

For each selected river segment, we set the dissolution rate of the flood basalt ($Na_{0.11}K_{0.01}Fe(II)_{0.14}Mg_{0.22}Ca_{0.22}Al_{0.38}Fe(III)_{0.05}SiTi_{0.02}O_{3.33}$) (59) in its watershed at 1 ton of basalt per hectare per year in the baseline scenario. In the sensitivity tests, two additional scenarios are employed: one with 0.5 ton of basalt per hectare per year and another with 1.5 tons of basalt per hectare per year. This basalt mineral stoichiometries stipulate that dissolution of 1 mol of basalt is equivalent to consuming 1.28 mol CO_2 from the atmosphere. Meantime, 1.28 mol DIC and 1.28 mol ALK (DIC:ALK = 1) along with the cations per mol of basalt dissolution, will enter the river segment. Coupling the forward ODE framework (Eq. 1–4) with specified basalt dissolution rates at each river segment, we track the dynamics of river chemistry (e.g., carbonate saturation state and carbon degassing) in each segment of each flow path for 2 years with a time step of 0.1 day. In addition to the river DIC, ALK, Ca, and salinity readily available from the ODE system, at each time step, we solve the complete carbonate system chemistry using the fast numerical routine proposed by Follows et al. (60), calculate the carbon degassing flux following Eq. 5 (with an atmospheric CO_2 concentration of 380 ppm), and derive the calcite saturation state following Eq. S1. For each flow path, we calculate the cumulative carbon degassing fluxes across the whole downstream segments through time (Fig. 2B). We define the cumulative carbon leakage for each flow path following Eq. S10.

$$L_{carbon}(\%) = \frac{\sum_0^t \left(\sum_i^k F_{degass\_ERW_i} - \sum_i^k F_{degass\_background_i}\right)}{\sum_0^t F_{DIC_{ERW}}} \cdot 100 \ (S10)$$

Where $L_{carbon}(\%)$ represents the proportion of the cumulative carbon leakage with time, t represents the model time, i represents the individual segment number, k represents the number of segments in the flow path, F_{degass_ERW} represents the carbon degassing flux of each segment following the application of EW, $F_{degass\_background}$ represents the carbon degassing flux of each segment before EW, and $F_{DIC_{ERW}}$ represents the DIC flux input from EW.

Data and code availability

The GRADES network and its associated properties (e.g., watershed area, discharge, connectivity) are from here:
https://www.reachhydro.org/home/params/merit-basins

The global monthly river pCO_2 values can be found at the link below. The file downloaded from this website is a ZIP file, which can be extracted using the default unzipping software on both Windows and Mac systems.
https://datadryad.org/stash/dataset/doi:10.5061/dryad.d7wm37pz9
The DRN model will adhere to the GNU General Public License (GPL) standard and will be open source upon acceptance of the paper.

Acknowledgements

The authors want to acknowledge support from the Partnership for an Advanced Computing Environment (PACE) at the Georgia Institute of Technology, the Yale Center for Research Computing, and the Yale Center for Natural Carbon Capture (YCNCC). Portions of this research were conducted with the advanced computing resources provided by Texas A&M High Performance Research Computing. SZ, NJP, and CTR acknowledge funding from the DOE Earth shots award (#DE-SC0024709).

References

1. National Academies of Sciences, Engineering, and Medicine, *Negative Emissions Technologies and Reliable Sequestration: A Research Agenda* (Washington, DC: The National Academies Press, 2019) https:/doi.org/10.17226/25259 (June 16, 2021).
2. K. Riahi, *et al.*, "2022: Mitigation pathways compatible with long-term goals" in *IPCC, 2022: Climate Change 2022: Mitigation of Climate Change. Contribution of Working Group III to the Sixth Assessment Report of the Intergovernmental Panel on Climate Change [P. R. Shukla*, J. Skea, *et al.*, Eds. (10, 2022).
3. J. Rogelj, *et al.*, Mitigation Pathways Compatible with 1.5°C in the Context of Sustainable Development. *IPCC*, 82 (2018).
4. L. T. Bach, S. J. Gill, R. E. M. Rickaby, S. Gore, P. Renforth, CO2 Removal With Enhanced Weathering and Ocean Alkalinity Enhancement: Potential Risks and Co-benefits for Marine Pelagic Ecosystems. *Front. Clim.* **1** (2019).
5. D. J. Beerling, *et al.*, Potential for large-scale CO_2 removal via enhanced rock weathering with croplands. *Nature* **583**, 242–248 (2020).
6. J. Hartmann, *et al.*, Enhanced chemical weathering as a geoengineering strategy to reduce atmospheric carbon dioxide, supply nutrients, and mitigate ocean acidification. *Rev. Geophys.* **51**, 113–149 (2013).
7. Y. Kanzaki, N. J. Planavsky, C. T. Reinhard, New estimates of the storage permanence and ocean co-benefits of enhanced rock weathering. *PNAS Nexus* **2**, pgad059 (2023).
8. P. Renforth, C.-L. Washbourne, J. Taylder, D. A. C. Manning, Silicate Production and Availability for Mineral Carbonation. *Environ. Sci. Technol.* **45**, 2035–2041 (2011).
9. S. H. Baek, *et al.*, Impact of Climate on the Global Capacity for Enhanced Rock Weathering on Croplands. *Earths Future* **11**, e2023EF003698 (2023).
10. L. L. Taylor, *et al.*, Enhanced weathering strategies for stabilizing climate and averting ocean acidification. *Nat. Clim. Change* **6**, 402–406 (2016).
11. S. Zhang, *et al.*, River chemistry constraints on the carbon capture potential of surficial enhanced rock weathering. *Limnol. Oceanogr.* **67**, S148–S157 (2022).
12. D. J. Beerling, *et al.*, Farming with crops and rocks to address global climate, food and soil security. *Nat. Plants*, 1 (2018).
13. E. Blanc-Betes, *et al.*, In silico assessment of the potential of basalt amendments to reduce N2O emissions from bioenergy crops. *GCB Bioenergy* **13**, 224–241 (2021).
14. I. Chiaravalloti, *et al.*, Mitigation of soil nitrous oxide emissions during maize production with basalt amendments. *Front. Clim.* **5** (2023).
15. W. J. Knapp, E. T. Tipper, The efficacy of enhancing carbonate weathering for carbon dioxide sequestration. *Front. Clim.* **4** (2022).

16. K. J. Harrington, R. G. Hilton, G. M. Henderson, Implications of the Riverine Response to Enhanced Weathering for CO2 removal in the UK. *Appl. Geochem.* **152**, 105643 (2023).
17. S. Liu, P. A. Raymond, Hydrologic controls on pCO2 and CO2 efflux in US streams and rivers. *Limnol. Oceanogr. Lett.* **3**, 428–435 (2018).
18. P. Lin, *et al.*, Global Reconstruction of Naturalized River Flows at 2.94 Million Reaches. *Water Resour. Res.* **55**, 6499–6516 (2019).
19. S. Liu, *et al.*, The importance of hydrology in routing terrestrial carbon to the atmosphere via global streams and rivers. *Proc. Natl. Acad. Sci.* **119**, e2106322119 (2022).
20. U.S. Geological Survey, National Water Information System data available on the World Wide Web (USGS Water Data for the Nation) (2016) (November 11, 2018).
21. A. J. Ulseth, *et al.*, Distinct air–water gas exchange regimes in low- and high-energy streams. *Nat. Geosci.* **12**, 259–263 (2019).
22. P. A. Raymond, *et al.*, Scaling the gas transfer velocity and hydraulic geometry in streams and small rivers. *Limnol. Oceanogr. Fluids Environ.* **2**, 41–53 (2012).
23. R. O. Hall Jr., A. J. Ulseth, Gas exchange in streams and rivers. *WIREs Water* **7**, e1391 (2020).
24. P. A. Raymond, M. B. David, J. E. Saiers, The impact of fertilization and hydrology on nitrate fluxes from Mississippi watersheds. *Curr. Opin. Environ. Sustain.* **4**, 212–218 (2012).
25. J. Strefler, T. Amann, N. Bauer, E. Kriegler, J. Hartmann, Potential and costs of carbon dioxide removal by enhanced weathering of rocks. *Environ. Res. Lett.* **13**, 034010 (2018).
26. T. Reershemius, *et al.*, Initial Validation of a Soil-Based Mass-Balance Approach for Empirical Monitoring of Enhanced Rock Weathering Rates. *Environ. Sci. Technol.* **57**, 19497–19507 (2023).
27. C. Neal, Calcite saturation in eastern UK rivers. *Sci. Total Environ.* **282–283**, 311–326 (2002).
28. D. L. Suarez, Calcite supersaturation and precipitation kinetics in the Lower Colorado River, All-American Canal and East Highline Canal. *Water Resour. Res.* **19**, 653–661 (1983).
29. K. Szramek, L. M. Walter, Impact of Carbonate Precipitation on Riverine Inorganic Carbon Mass Transport from a Mid-continent, Forested Watershed. *Aquat. Geochem.* **10**, 99–137 (2004).
30. K. S. Aho, P. A. Raymond, Differential Response of Greenhouse Gas Evasion to Storms in Forested and Wetland Streams. *J. Geophys. Res. Biogeosciences* **124**, 649–662 (2019).
31. J. D. Schade, J. Bailio, W. H. McDowell, Greenhouse gas flux from headwater streams in New Hampshire, USA: Patterns and drivers. *Limnol. Oceanogr.* **61**, S165–S174 (2016).
32. B. Lehner, G. Grill, Global river hydrography and network routing: baseline data and new approaches to study the world's large river systems. *Hydrol. Process.* **27**, 2171–2186 (2013).
33. S. A. Comer-Warner, *et al.*, Thermal sensitivity of CO2 and CH4 emissions varies with streambed sediment properties. *Nat. Commun.* **9**, 2803 (2018).
34. P. Romeijn, S. A. Comer-Warner, S. Ullah, D. M. Hannah, S. Krause, Streambed Organic Matter Controls on Carbon Dioxide and Methane Emissions from Streams. *Environ. Sci. Technol.* **53**, 2364–2374 (2019).
35. P. Renforth, G. Henderson, Assessing ocean alkalinity for carbon sequestration. *Rev. Geophys.* **55**, 636–674 (2017).

36. T. Maavara, *et al.*, Watershed DOC uptake occurs mostly in lakes in the summer and in rivers in the winter. *Limnol. Oceanogr.* **68**, 735–751 (2023).
37. S. Wang, *et al.*, The community-centered freshwater biogeochemistry model unified RIVE v1.0: a unified version for water column. *Geosci. Model Dev.* **17**, 449–476 (2024).
38. E. S. Bernhardt, *et al.*, The metabolic regimes of flowing waters. *Limnol. Oceanogr.* **63**, S99–S118 (2018).
39. J.-P. Gattuso, J.-M. Epitalon, H. Lavigne, J. Orr, Seawater Carbonate Chemistry [R package seacarb version 3.2.16] (2021) (May 28, 2021).
40. R. E. Zeebe, D. Wolf-Gladrow, *CO_2 in seawater: Equilibrium, kinetics, isotopes, Volume 65*, 1 edition (Elsevier Science, 2001).
41. P. A. Raymond, *et al.*, Global carbon dioxide emissions from inland waters. *Nature* **503**, 355–359 (2013).
42. D. N. Karger, *et al.*, Climatologies at high resolution for the earth's land surface areas. *Sci. Data* **4**, 170122 (2017).
43. G. Ghiggi, V. Humphrey, S. I. Seneviratne, L. Gudmundsson, G-RUN ENSEMBLE: A Multi-Forcing Observation-Based Global Runoff Reanalysis. *Water Resour. Res.* **57**, e2020WR028787 (2021).
44. Y. Wang, *et al.*, Development of observation-based global multilayer soil moisture products for 1970 to 2016. *Earth Syst. Sci. Data* **13**, 4385–4405 (2021).
45. J. Hartmann, N. Moosdorf, The new global lithological map database GLiM: A representation of rock properties at the Earth surface. *Geochem. Geophys. Geosystems* **13**, Q12004 (2012).
46. M.-N. Tuanmu, W. Jetz, A global 1-km consensus land-cover product for biodiversity and ecosystem modelling. *Glob. Ecol. Biogeogr.* **23**, 1031–1045 (2014).
47. G. Amatulli, D. McInerney, T. Sethi, P. Strobl, S. Domisch, Geomorpho90m, empirical evaluation and accuracy assessment of global high-resolution geomorphometric layers. *Sci. Data* **7**, 162 (2020).
48. I. J. Larsen, D. R. Montgomery, H. M. Greenberg, The contribution of mountains to global denudation. *Geology* **42**, 527–530 (2014).
49. L. Poggio, *et al.*, SoilGrids 2.0: producing soil information for the globe with quantified spatial uncertainty. *SOIL* **7**, 217–240 (2021).
50. M. Zhao, F. A. Heinsch, R. R. Nemani, S. W. Running, Improvements of the MODIS terrestrial gross and net primary production global data set. *Remote Sens. Environ.* **95**, 164–176 (2005).
51. B. Pan, S. K. Lam, E. Wang, A. Mosier, D. Chen, New approach for predicting nitrification and its fraction of N2O emissions in global terrestrial ecosystems. *Environ. Res. Lett.* **16**, 034053 (2021).
52. L. Breiman, Random Forests. *Mach. Lang.* **45**, 5–32 (2001).
53. T. Hastie, R. Tibshirani, J. Friedman, *The elements of statistical learning: Data mining, inference, and prediction, second edition*, 2nd edition (Springer, 2016).
54. B. E, S. Zhang, C. T. Driscoll, T. Wen, Human and natural impacts on the U.S. freshwater salinization and alkalinization: A machine learning approach. *Sci. Total Environ.* **889**, 164138 (2023).
55. R Core Team, R: A language and environment for statistical computing. *R Found. Stat. Comput. Vienna Austria HttpswwwR-Proj.* (2017).

56. M. N. Wright, A. Ziegler, ranger: A Fast Implementation of Random Forests for High Dimensional Data in C++ and R. *J. Stat. Softw.* **77**, 1–17 (2017).
57. F. N. Fritsch, R. E. Carlson, Monotone Piecewise Cubic Interpolation. *SIAM J. Numer. Anal.* **17**, 238–246 (1980).
58. K. Soetaert, T. Petzoldt, R. W. Setzer, Solving Differential Equations in R: Package deSolve. *J. Stat. Softw.* **33**, 1–25 (2010).
59. L. Marini, *Geological Sequestration of Carbon Dioxide: Thermodynamics, Kinetics, and Reaction Path Modeling*, 1st edition (Elsevier Science, 2006).
60. M. J. Follows, T. Ito, S. Dutkiewicz, On the solution of the carbonate chemistry system in ocean biogeochemistry models. *Ocean Model.* **12**, 290–301 (2006).

Figures

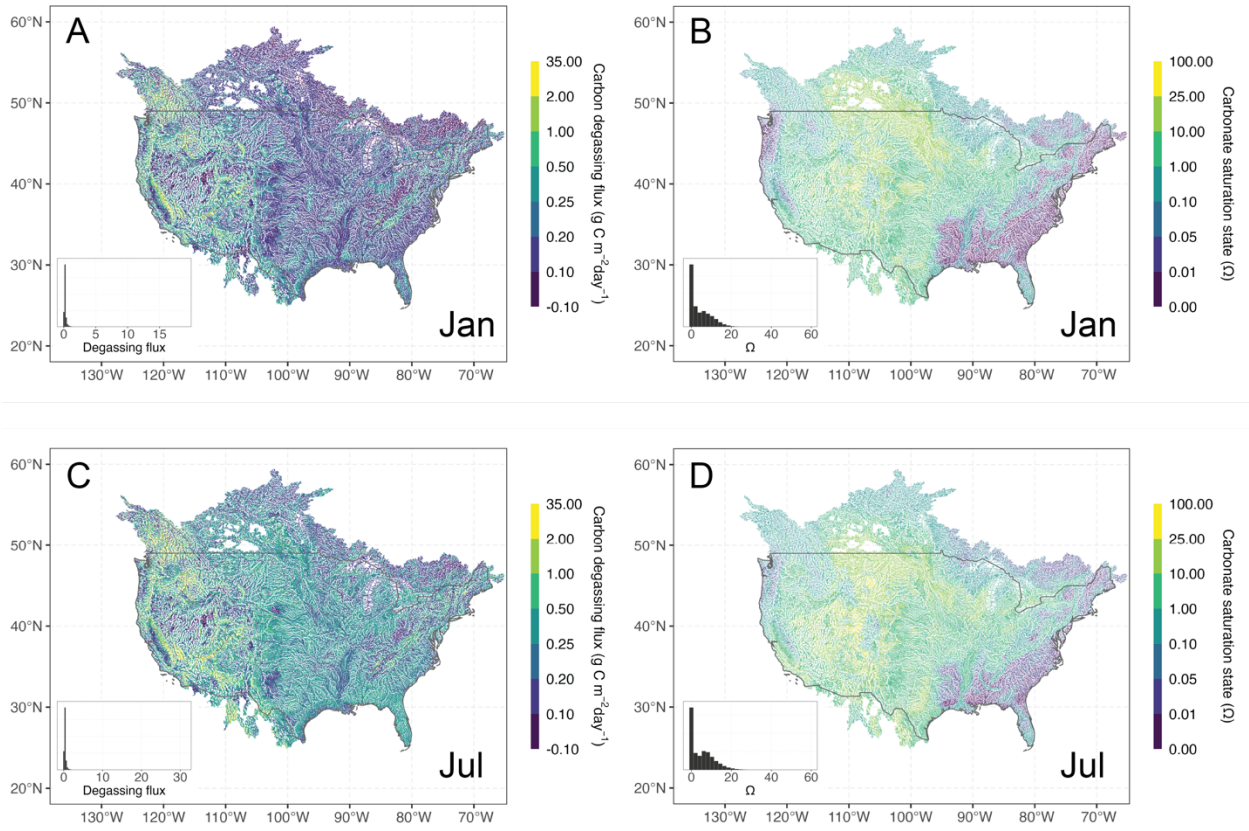

Figure 1. Predicted background carbon degassing flux and carbonate mineral (calcite) saturation state (Ω) for each river segment across the North America river network. (A) Carbon degassing flux in January (B) River Ω values in January (C) Carbon degassing flux in July (D) River Ω values in July. The lines represent the river segments within North America.

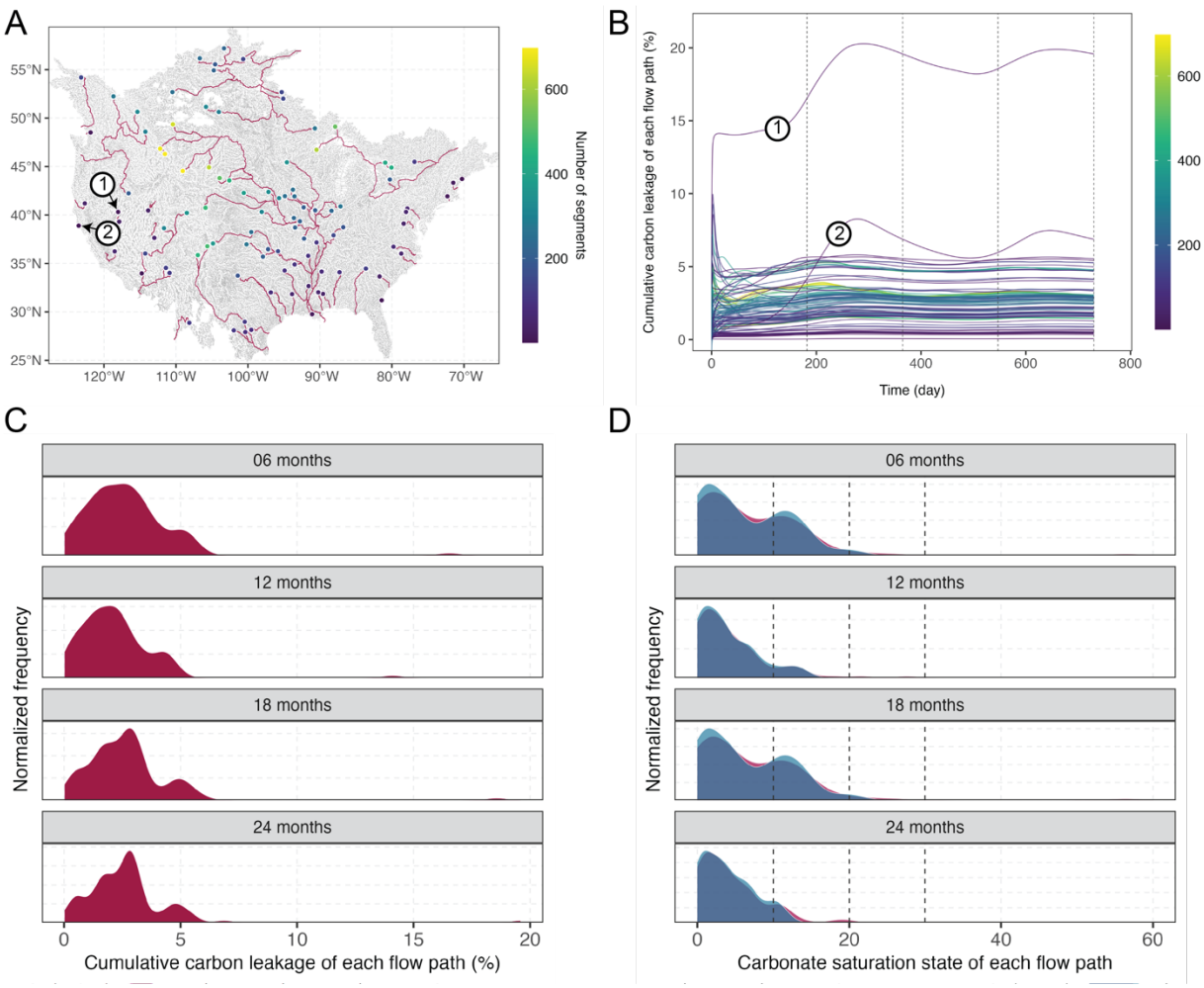

Figure 2. Changes in cumulative carbon leakage rate and carbonate mineral (calcite) saturation state in the downstream in response to the incoming EW fluxes in North American watersheds. (A) EW application sites (100 random sites) and their corresponding downstream segments. (B) Cumulative carbon leakage rate through time across the whole downstream segments of each flow path for each EW application site. (C) Frequency distribution of the cumulative carbon leakage of the whole flow path through time. (D) Frequency distribution of median carbonate saturation state of river segments for each flow path through time. The two symbols (1 and 2) in panel A and B represent the two flow paths with the highest leakage rates. Dashed lines in panel B represent 6 months, 12 months, 18 months, and 24 months from left to right. Dashed lines in panel D represent Ω values of 10, 20, and 30 from left to right. Blue distributions in panel D indicate conditions prior to EW application, while red distributions represent conditions after EW application.

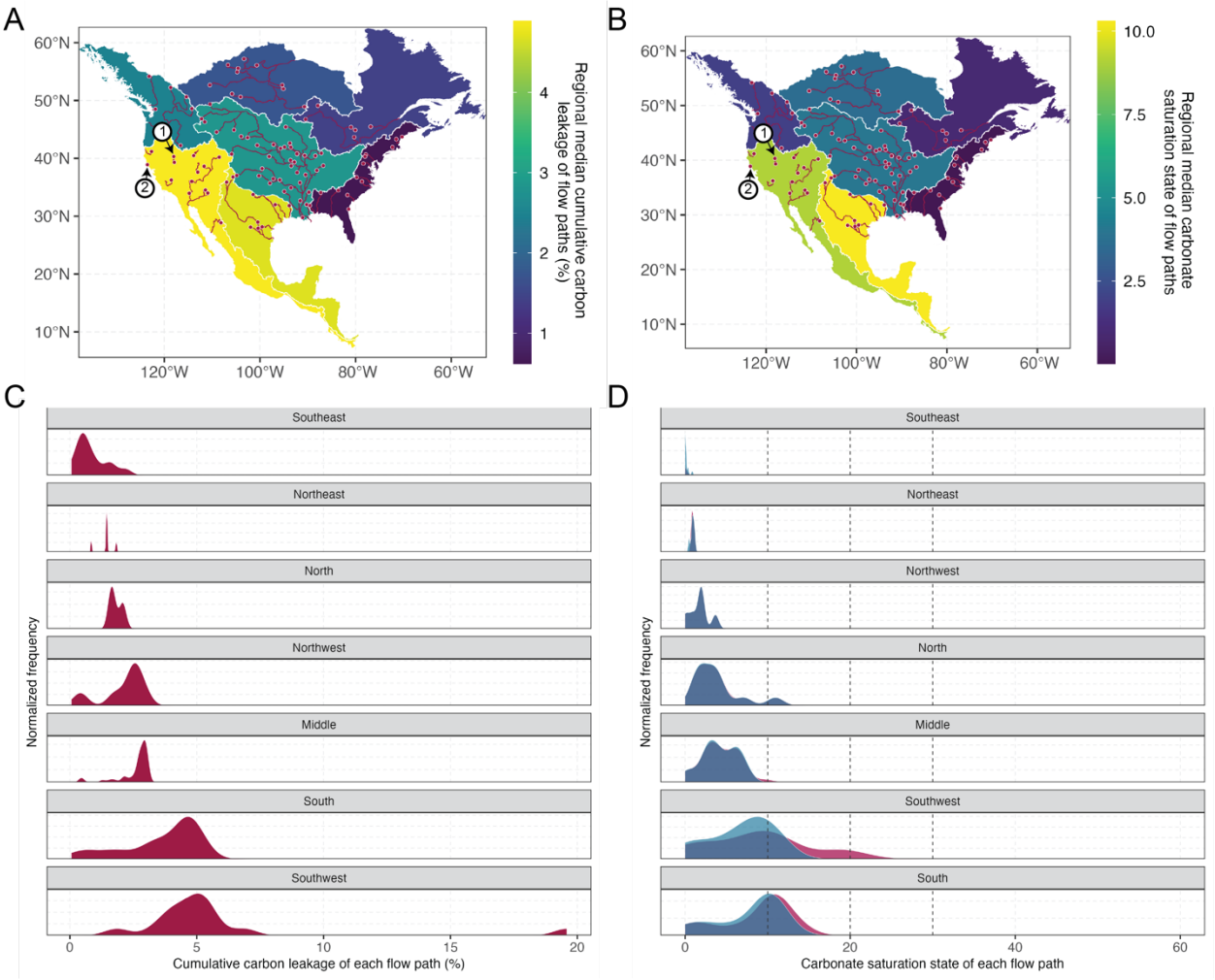

Figure 3. Spatial differences in river network responses to incoming EW fluxes in the North America watersheds. (A) Median cumulative carbon leakage of the whole flow path in each region after 24 months. (B) Median carbonate mineral (calcite) saturation state of all river segments in each region after 24 months. (C) Frequency distribution of the cumulative carbon leakage of the whole flow path in each region after 24 months. (D) Frequency distribution of carbonate saturation state of all flow paths in each region after 24 months. The two symbols (1 and 2) in panel A and B represent the two flow paths with the highest leakage rates. Dashed lines in panel D represent Ω values of 10, 20, and 30 from left to right. Blue distributions in panel D indicate conditions prior to EW application, while red distributions represent conditions after EW application.

Supporting Information for

Constraining carbon loss from rivers following terrestrial enhanced rock weathering

Shuang Zhang[a,1], Christopher T. Reinhard[b], Shaoda Liu[c], Yoshiki Kanzaki[b], Noah J. Planavsky[d,e]

[a]Department of Oceanography, Texas A&M University, College Station, TX, USA
[b]School of Earth and Atmospheric Sciences, Georgia Institute of Technology, Atlanta, GA, USA
[c]School of Environment, Beijing Normal University, Beijing, China
[d]Department of Earth and Planetary Sciences, Yale University, New Haven, CT, USA
[e]Yale Center for Natural Carbon Capture, Yale University, New Haven, CT, USA

***Corresponding author**: Shuang Zhang
Email: shuang-zhang@tamu.edu

This PDF file includes:

Figures S1 to S21

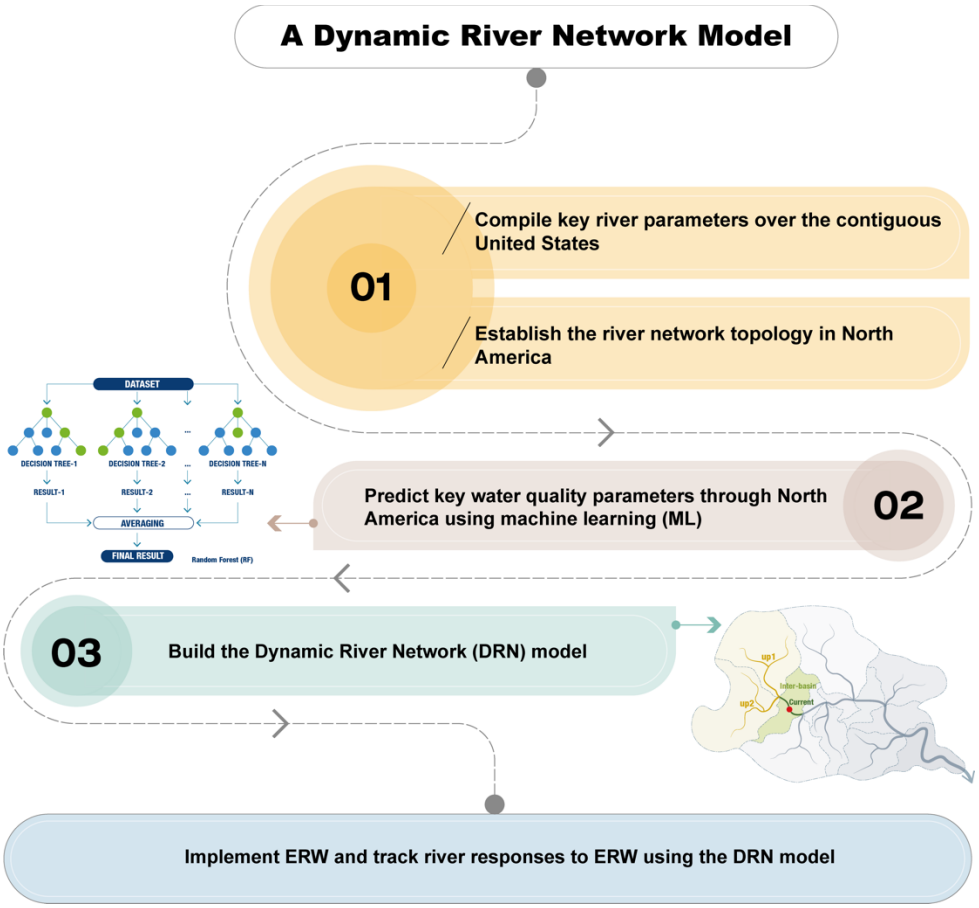

Figure S1. The workflow of building the dynamic river network model.

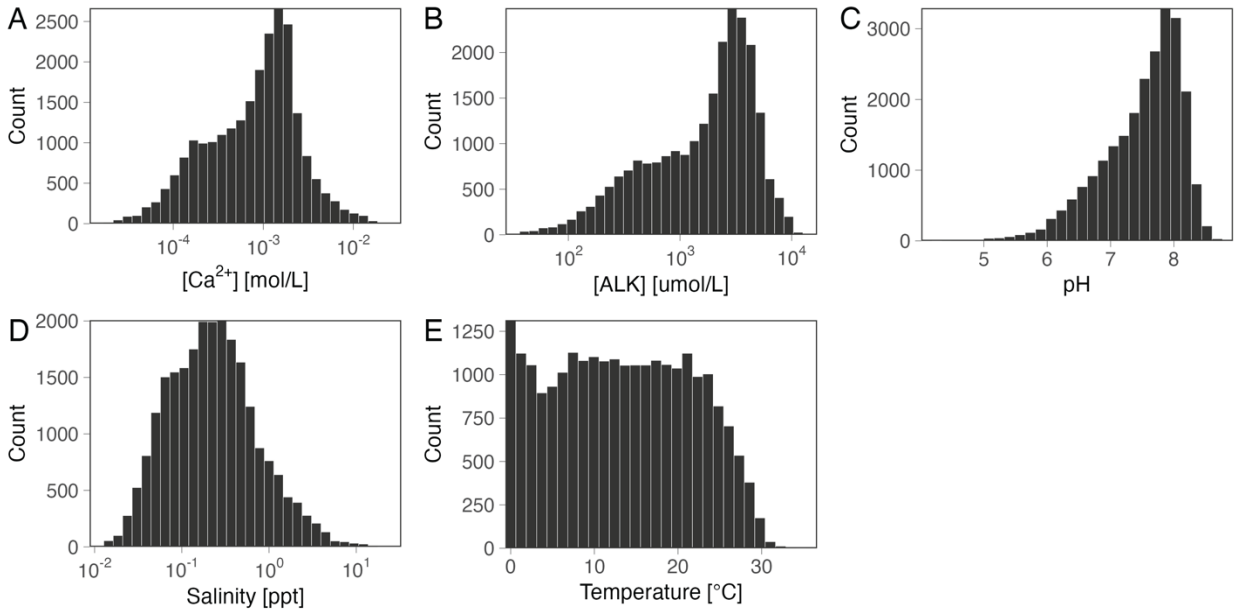

Figure S2. Frequency distributions of collected solute, salinity, and temperature data from USGS for river data in the U.S. Shown are the key parameters for solving the carbonate system, including (A) dissolved Ca^{2+}, (B) ALK, (C) pH, (D) salinity, and (E) temperature.

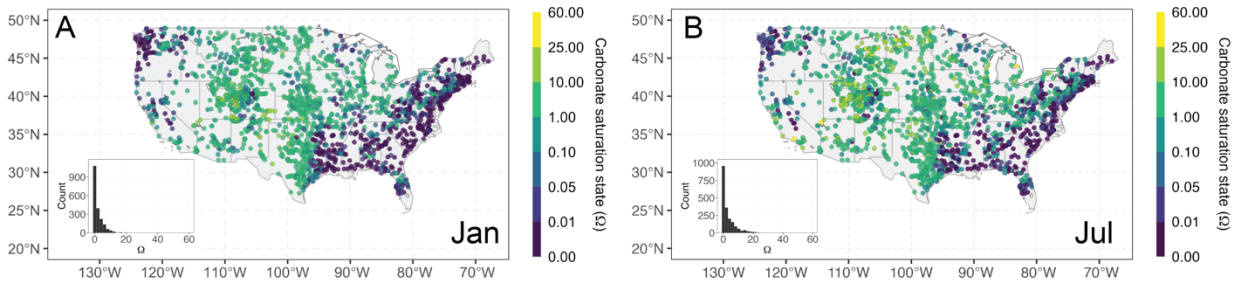

Figure S3. River site locations and distributions of calcite saturation state (Ω) in January (A) and July (B) across the coterminous U.S.

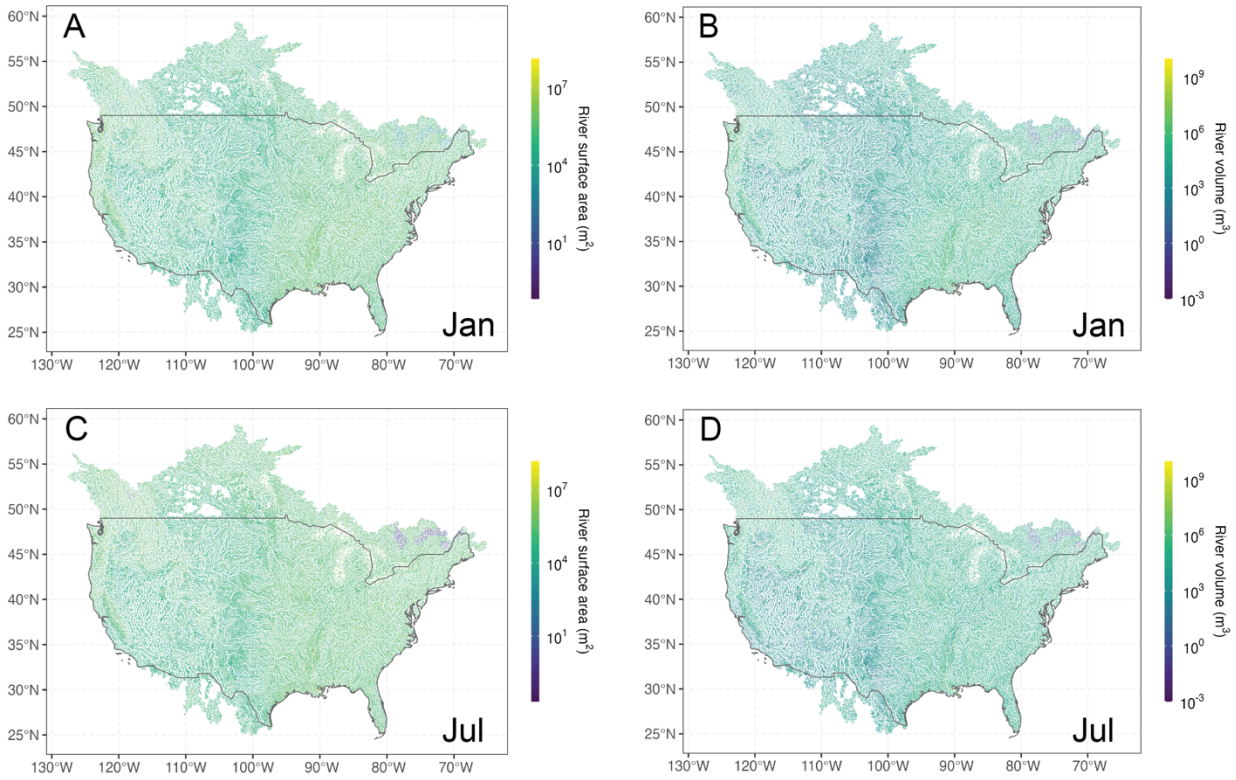

Figure S4. Reconstructed River segment surface area and volume from the GRADES database for January and July.

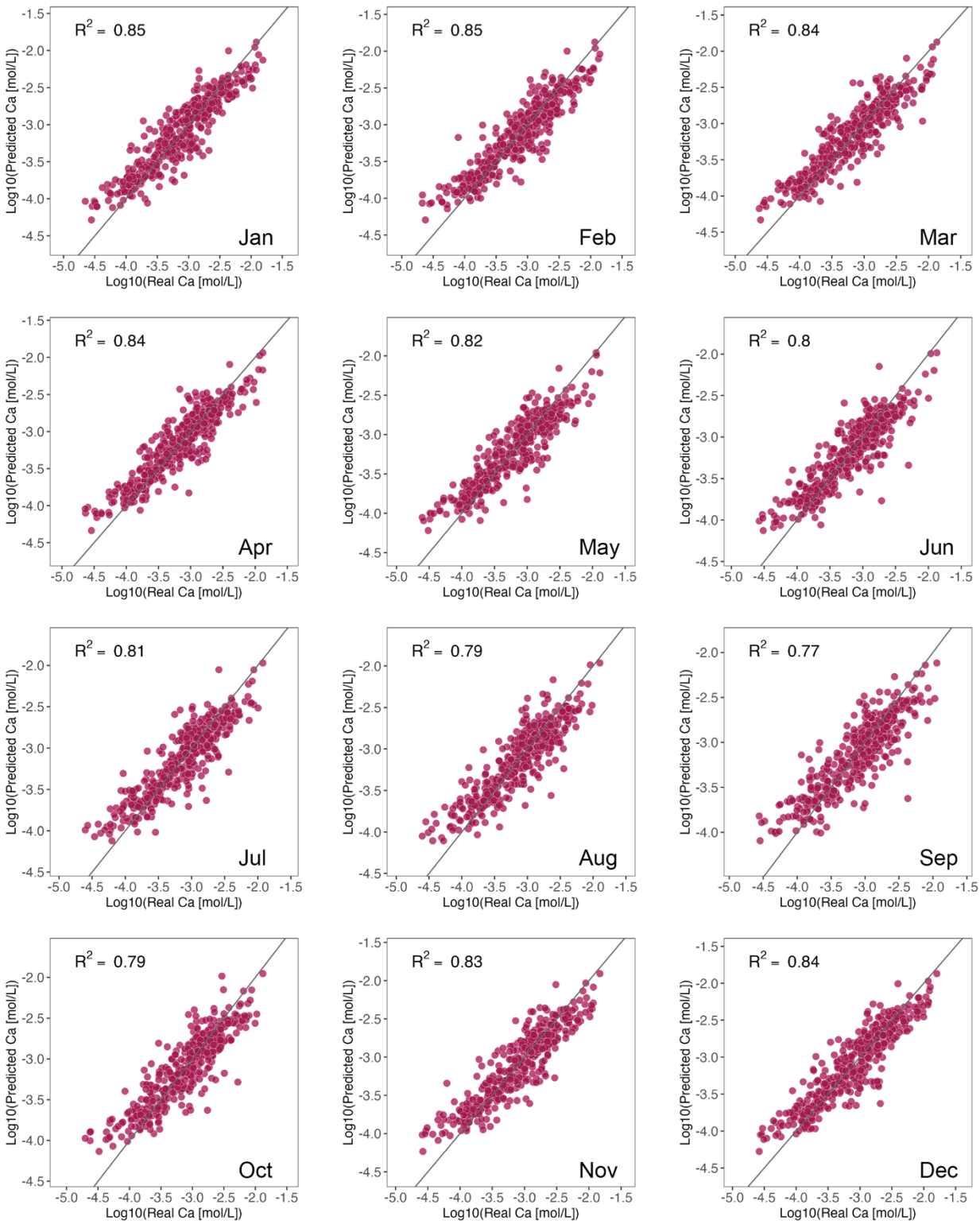

Figure S5. The correspondence of ML-predicted Ca concentration and the real Ca concentration for the test dataset at each month.

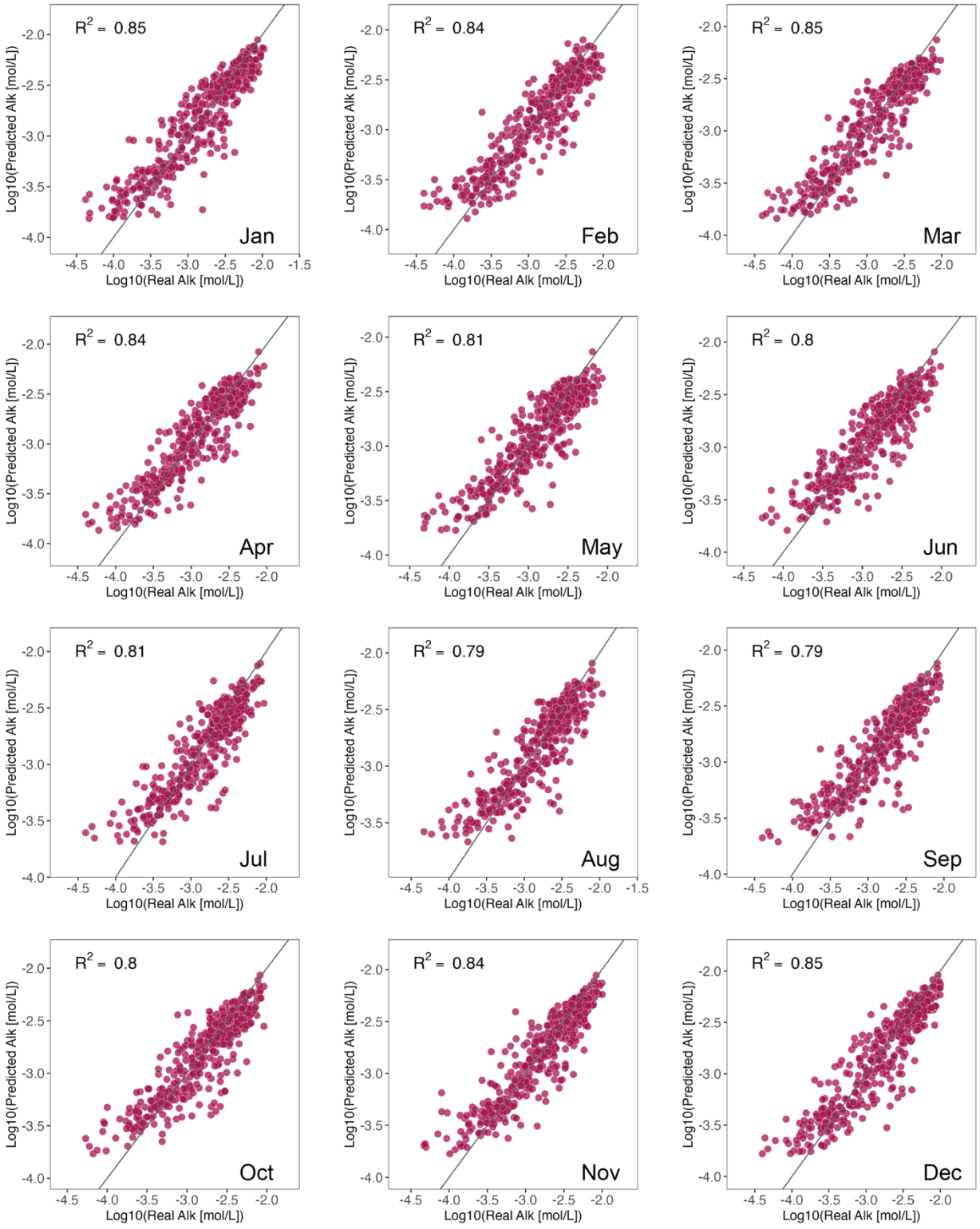

Figure S6. The correspondence of ML-predicted ALK and the real ALK for the test dataset at each month.

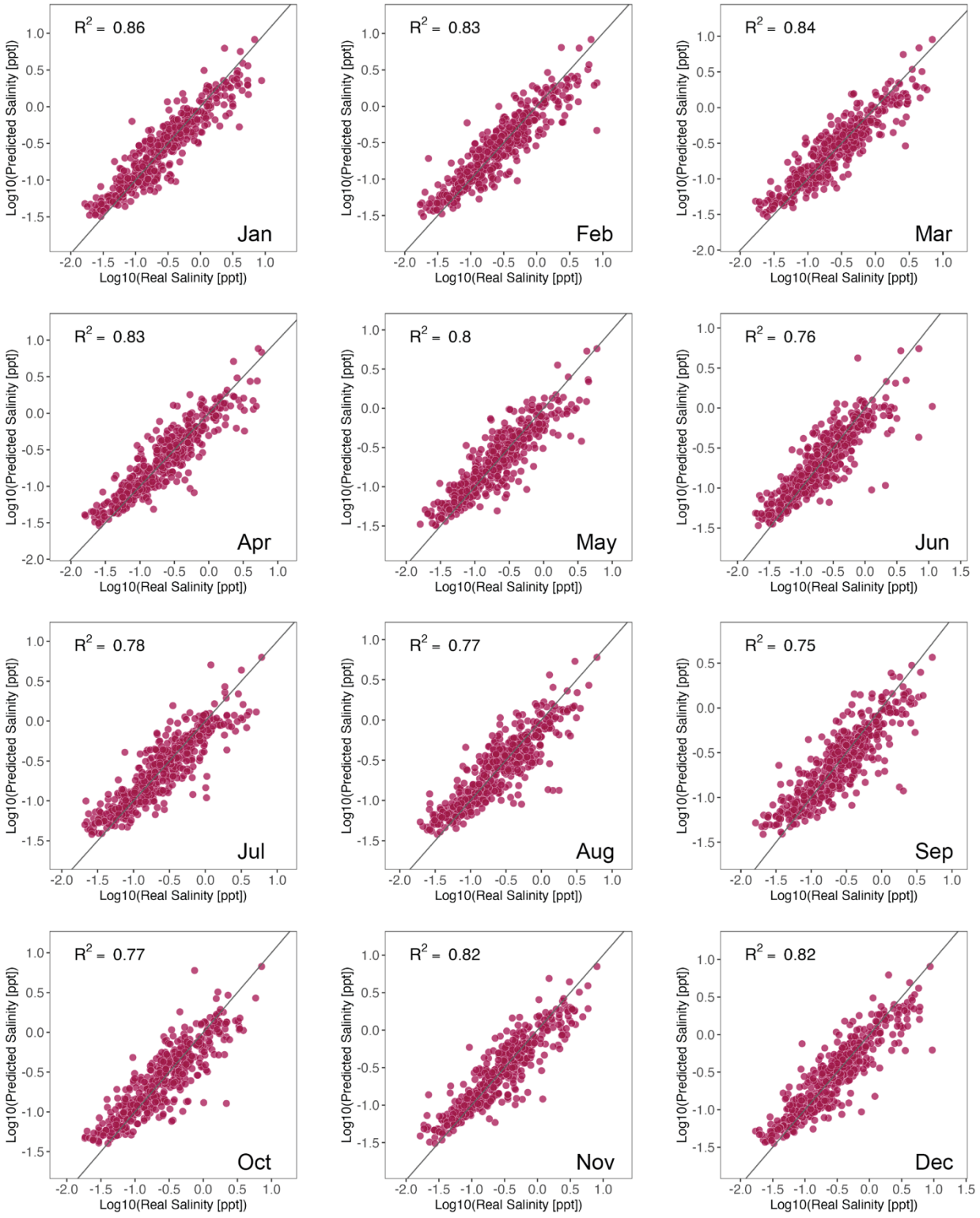

Figure S7. The correspondence of ML-predicted salinity and the real salinity for the test dataset at each month.

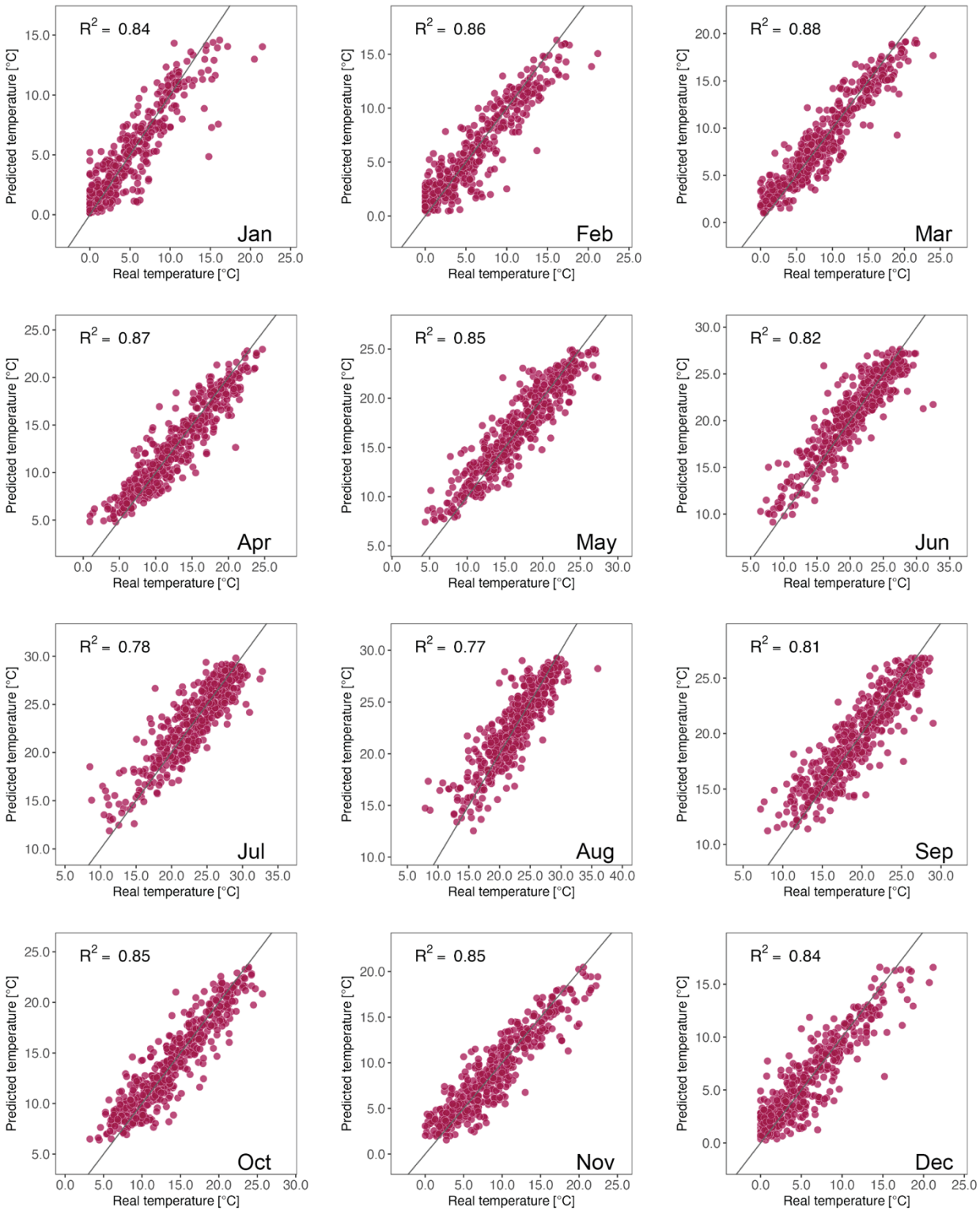

Figure S8. The correspondence of ML-predicted water temperature and the real water temperature for the test dataset at each month.

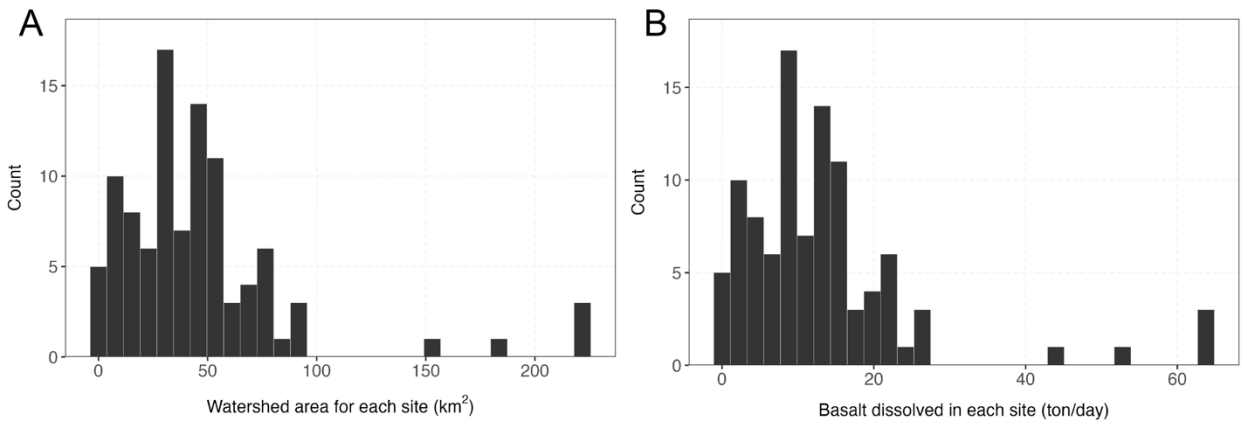

Figure S9. Watershed areas of the headwater segment (A) and basalt dissolution rate (B) for the 100 application sites across North America.

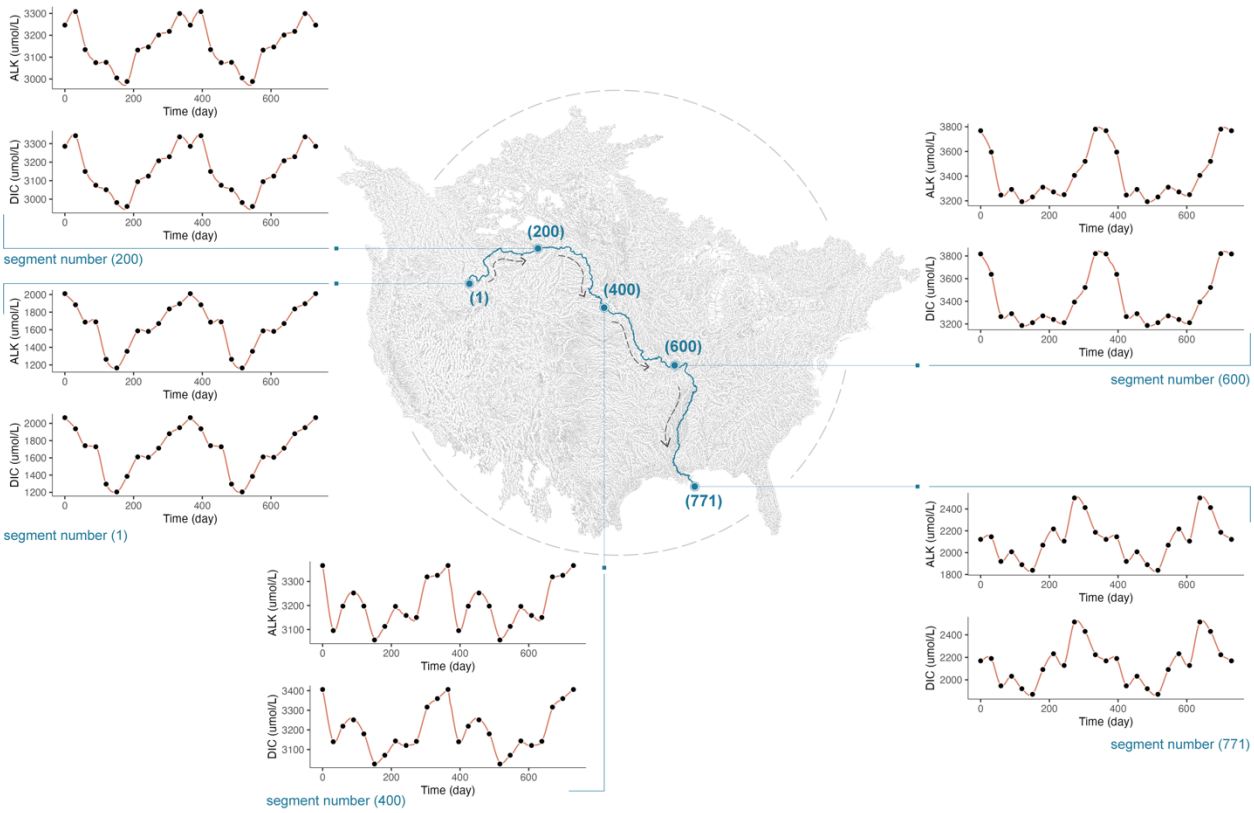

Figure S10. DRN model reconstruction of background chemistry of the Mississippi River. From top to bottom on the map, the river segment numbers are 1 (the headwater), 200, 400, 600, and 771 (the Mississippi river outlet) sequentially. Background monthly river chemistry (DIC and ALK) is represented by the black dots and the model simulation result is represented by the red line.

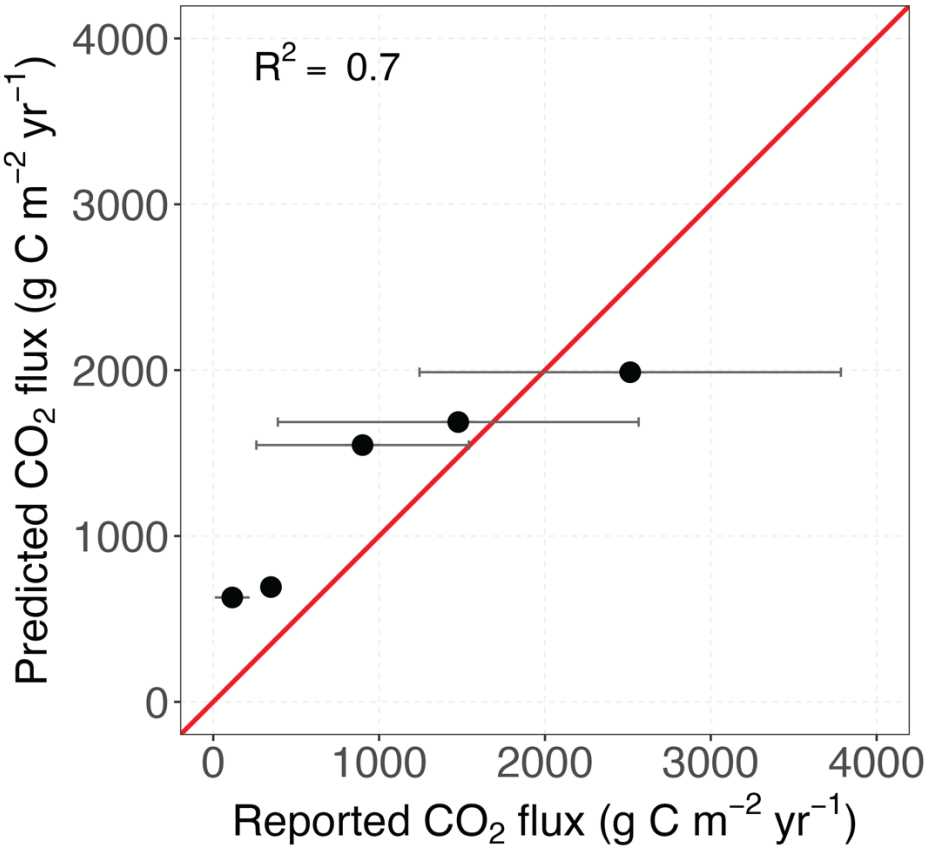

Fig S11. Comparing predicted CO_2 degassing per water surface area with values reported in the literature. The reported values are for the rivers in central Connecticut and New Hampshire (references can be found in the main text). We matched the river sites mentioned in the literature with the nearest river segments in our model. Then, we compared the average monthly or annual carbon degassing flux (as resolved by the reports) of the sites located on the same river segment with our model's outcomes. The error bar represents 1 standard deviation of the reported carbon degassing across multiple sites that are snapped to the same river segment.

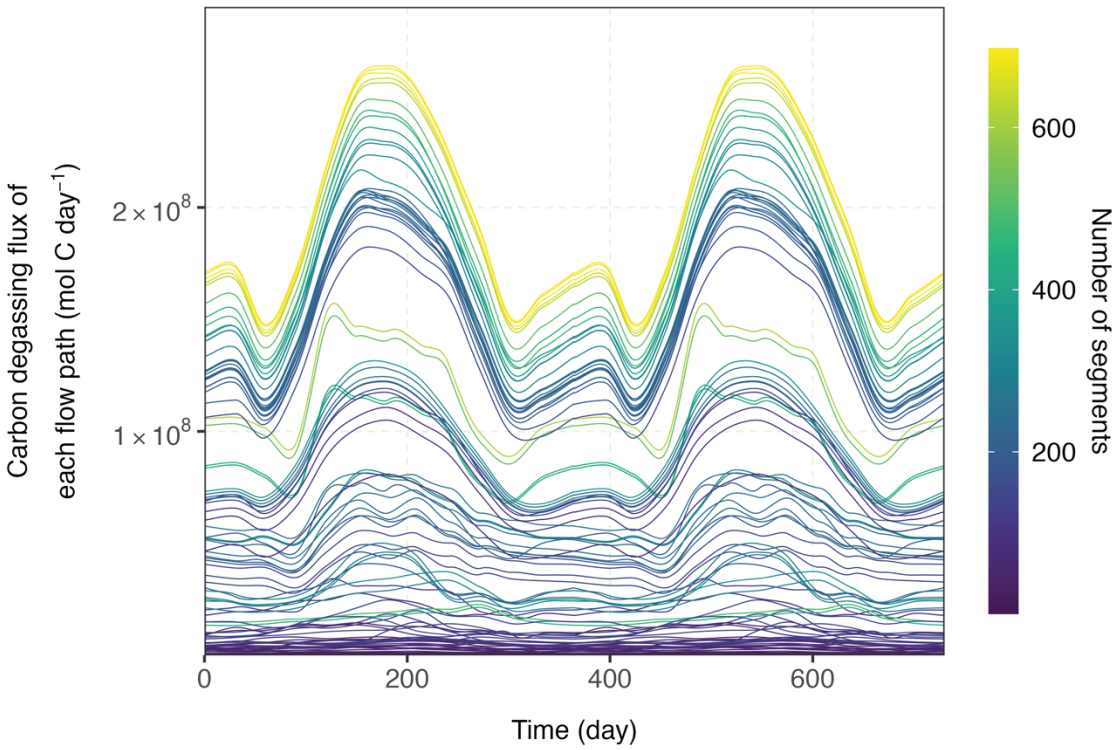

Figure S12. Carbon degassing flux through time across the whole downstream segments of each flow path for the 100 ERW application sites.

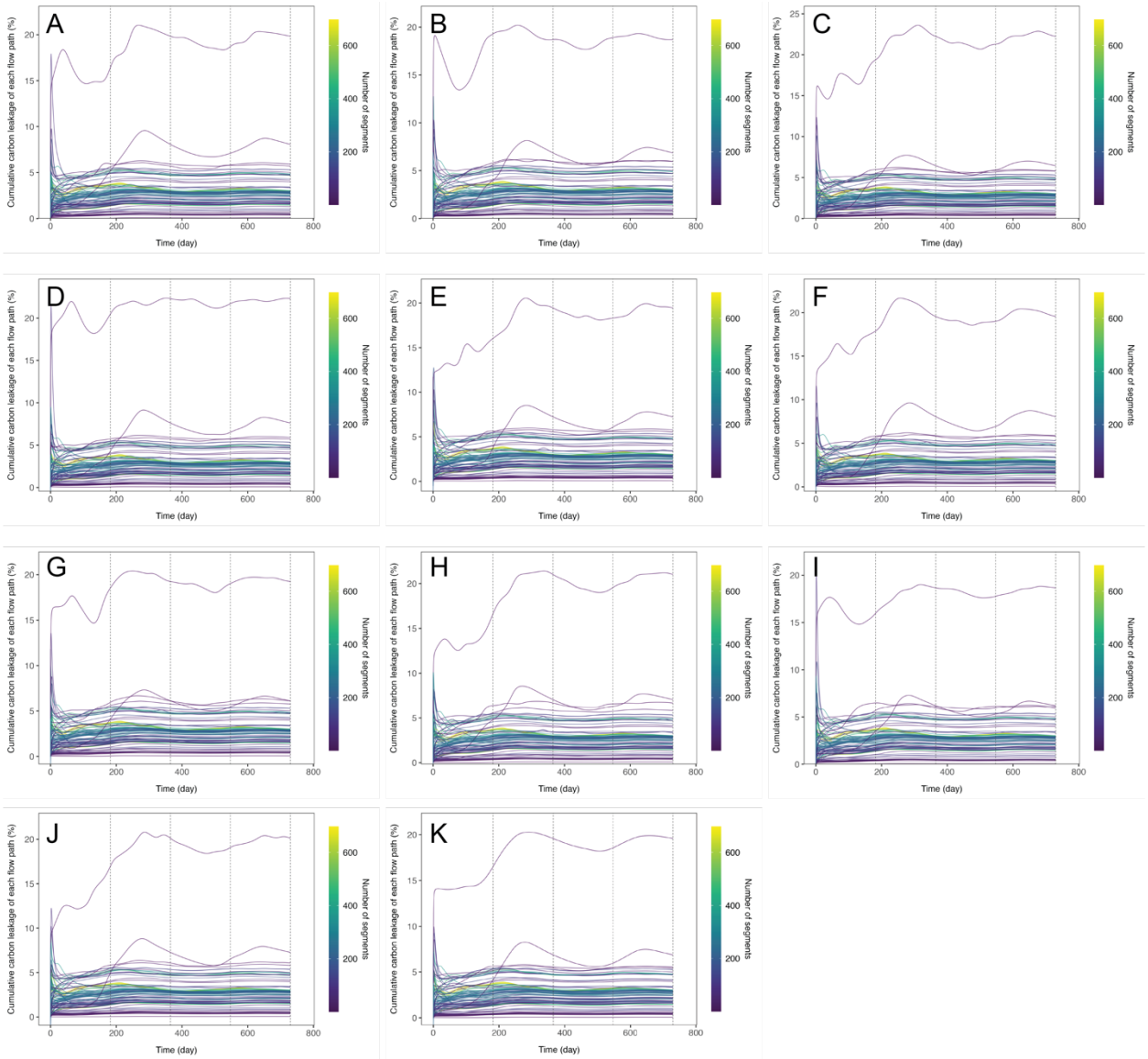

Figure S13. Sensitivity tests of the cumulative carbon leakage rate through time across the whole downstream segments of each flow path for each ERW application site. (A-J) The 10 sensitivity test results. (K) The baseline results. Note that the baseline results are shown here for comparison with the sensitivity test results.

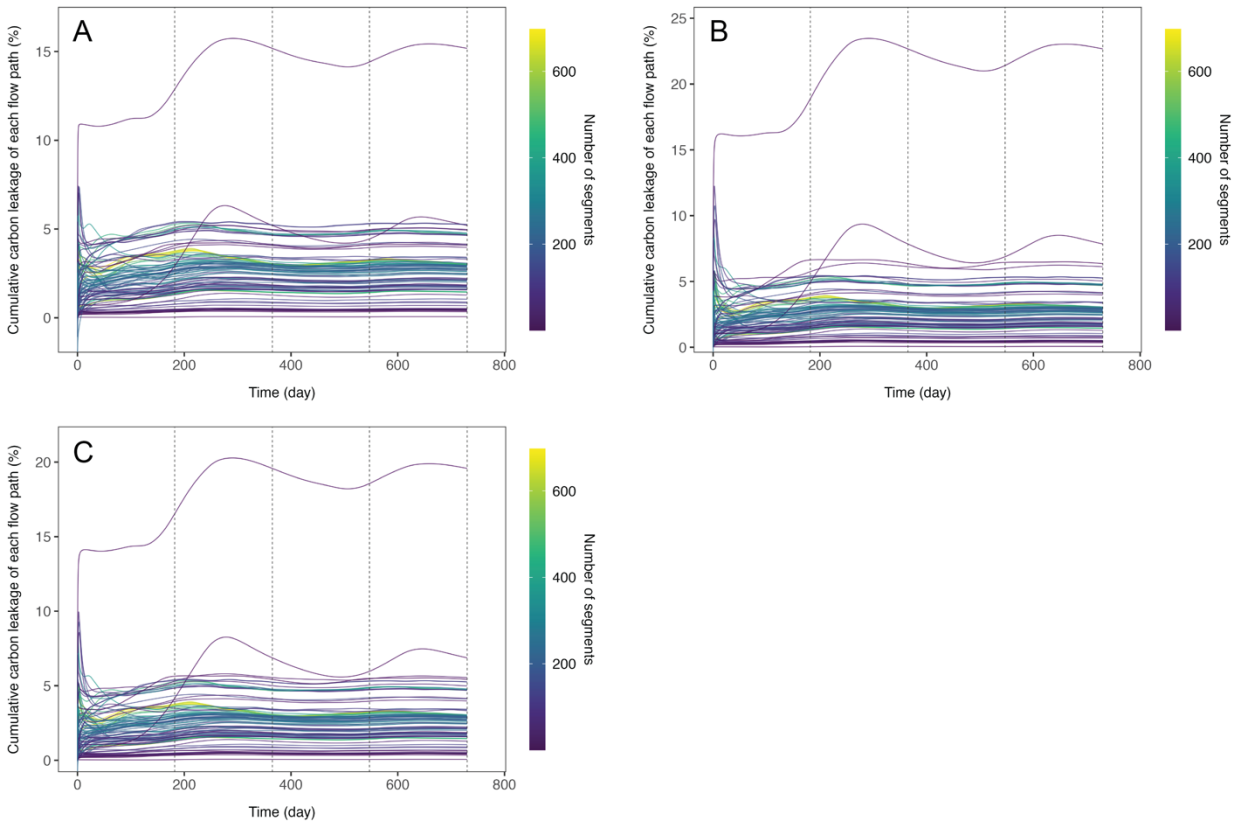

Figure S14. Different scenarios (low, high, and baseline) of the cumulative carbon leakage rate through time across the whole downstream segments of each flow path for each ERW application site. (A) The low scenario with 0.5 ton of basalt dissolution per hectare per year. (B) The high scenario with 1.5 ton of basalt dissolution per hectare per year. (C) The baseline scenario with 1 ton of basalt dissolution per hectare per year. Note that the baseline scenario is shown here for comparison with the other two scenarios.

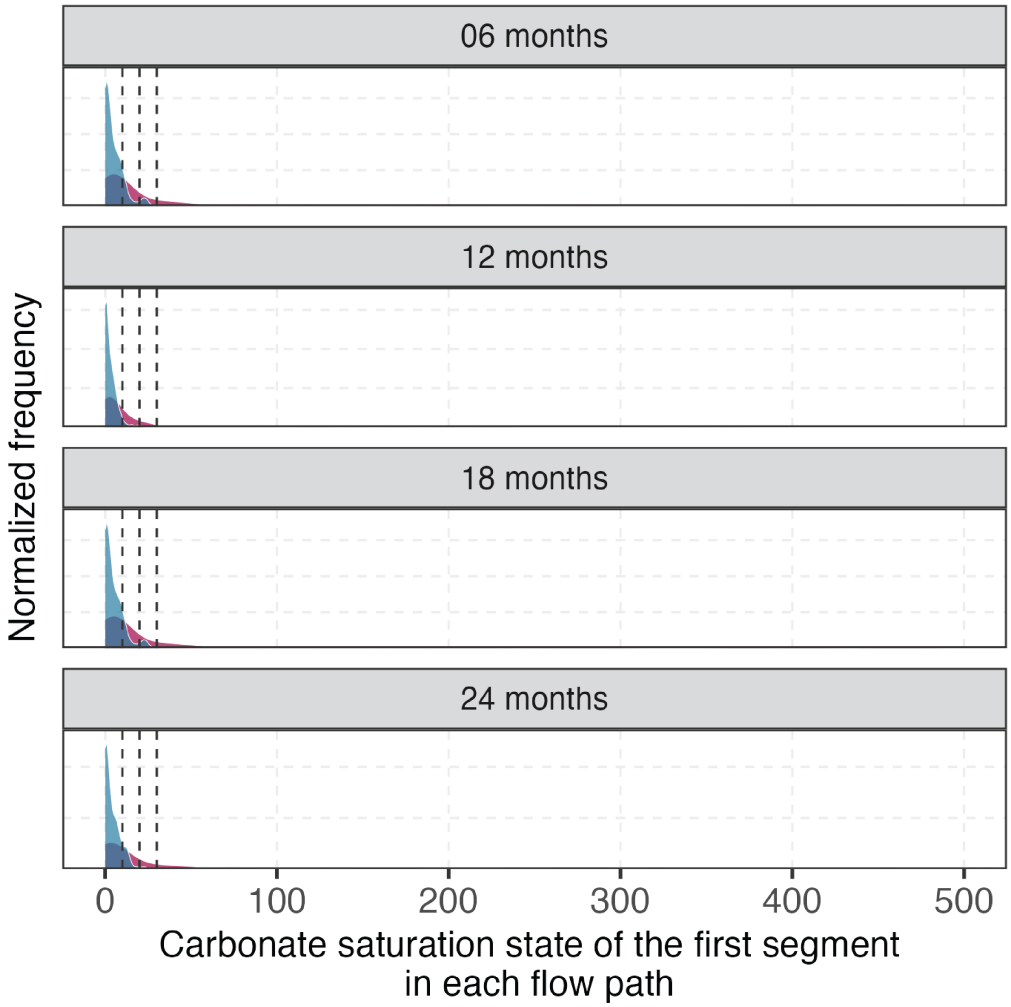

Figure S15. Frequency distribution of carbonate saturation state of the first river segment for each flow path through time. Dashed lines represent Ω values of 10, 20, and 30 from left to right. Blue distributions indicate conditions prior to EW application, while red distributions represent conditions after EW application. As the distribution of Ω values is extremely right-skewed, extreme Ω values bigger than 200 (~10% of the data) are not plotted to help visualization.

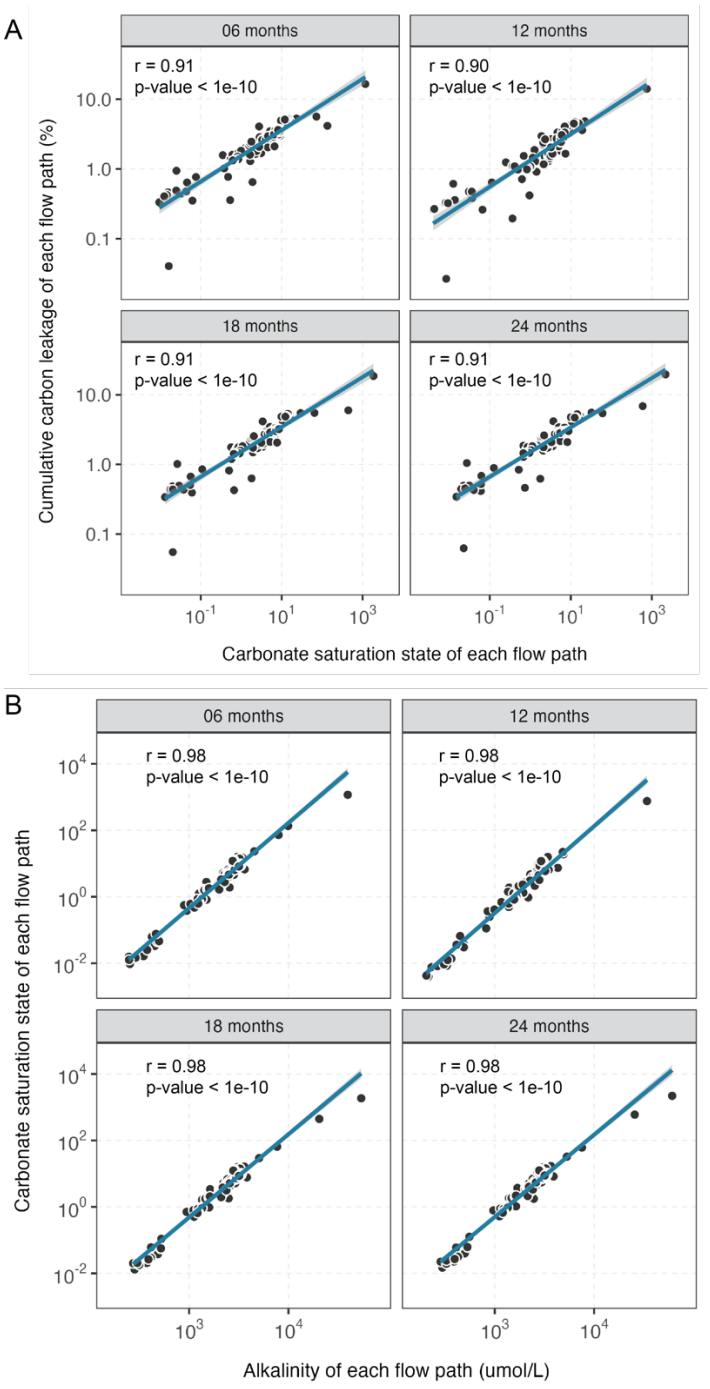

Figure S16. Correlation between the cumulative carbon leakage rate, the median carbonate saturation state, and the median alkalinity of segments for each flow path over durations of 6, 12, 18, and 24 months. Here, the carbonate saturation state represents the average of the median carbonate saturation states of segments for each flow path from day 0 to the specified duration. The alkalinity represents the average of the median alkalinity of segments for each flow path from day 0 to the specified duration The correlation coefficient (r) and the p-value are also shown.

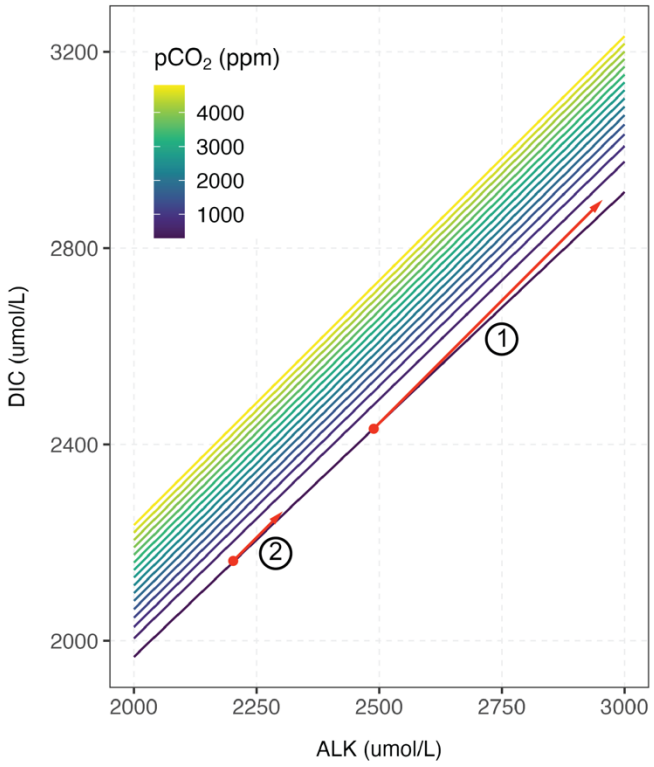

Figure S17. Thermodynamic relations of alkalinity (ALK), total dissolved inorganic carbon (DIC) and the equilibrium pCO_2 in river (µatm) plotted for salinity=1 and temperature=12°C. The contour lines depict the correlation between ALK and DIC for individual pCO_2 values ranging from 300 to 5000 µatm, a range typical for the river systems in North America. The two red arrows in panel b illustrate the input of DIC and ALK at a 1:1 ratio into the river. The length of the arrow represents the quantity of DIC and ALK introduced into the river. A longer arrow, denoted by symbol 1, signifies a larger input flux and an associated greater increase in pCO_2 than a shorter arrow, represented by symbol 2.

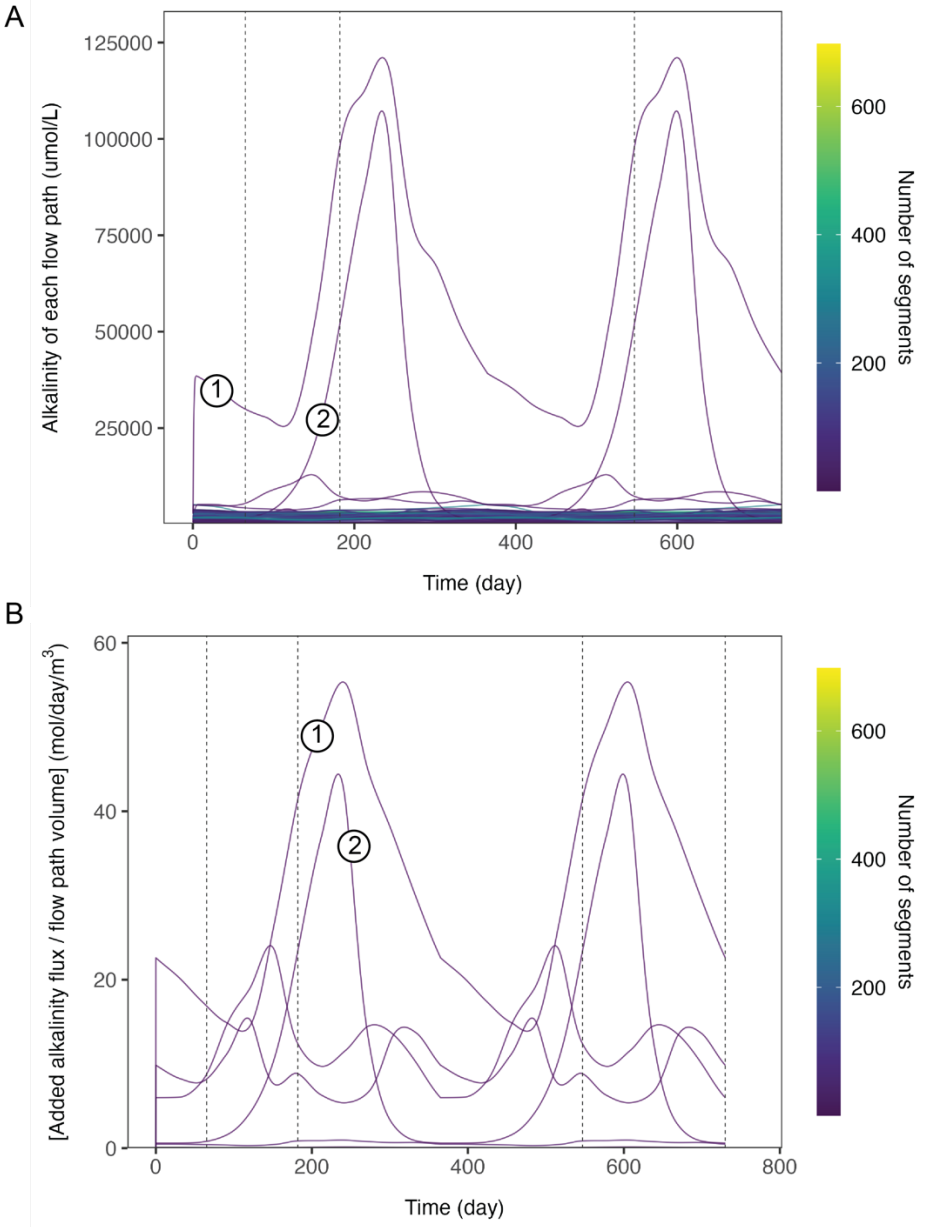

Figure S18. Alkalinity and the alkalinity/volume ratio through time of each flow path for each ERW application site. (A) Median alkalinity of river segments for each flow path through time for each ERW application site. (B) The ratio of alkalinity input flux from the basalt dissolution to the total volume of river segments for each flow path through time for each ERW application site. The two symbols in panel A and B represent the two flow paths with the highest leakage rates (see Fig. 2B). Dashed lines in panel A and B represent 6 months, 12 months, 18 months, and 24 months from left to right.

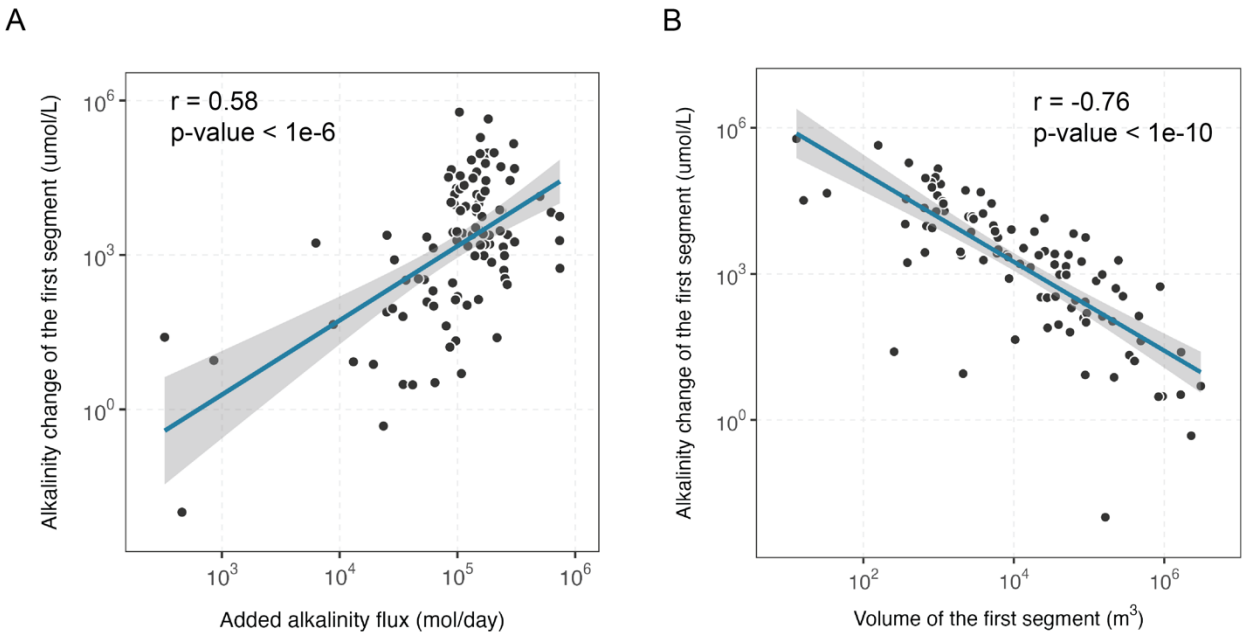

Figure S19. (A) Correlation between the alkalinity change of the first river segment (relative to its concurrent background state) and the added alkalinity flux for each flow path over duration of 1 day. (B) Correlation between the alkalinity change of the first river segment (relative to its concurrent background state) and the volume of the first segment over duration of 1 day. The correlation coefficient (r) and the p-value are also shown.

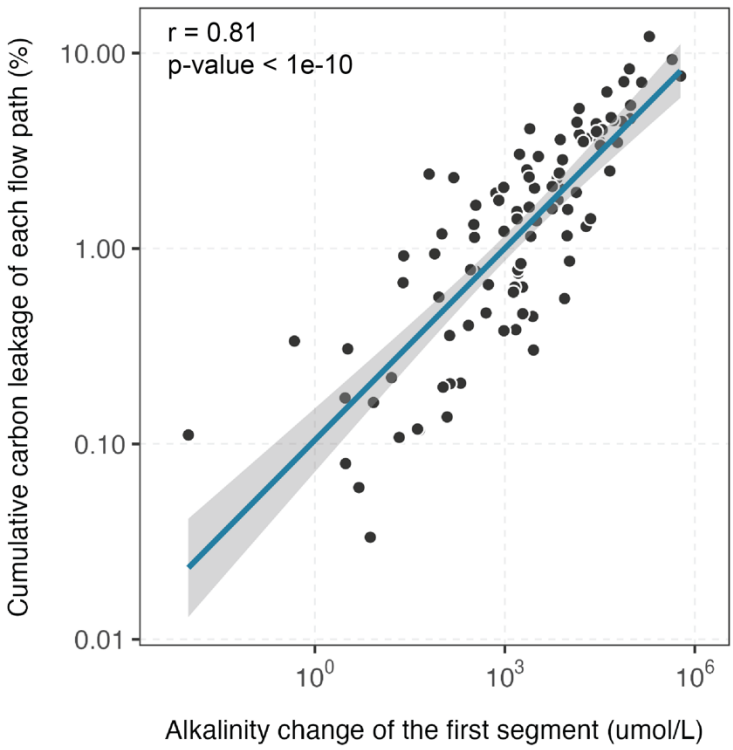

Figure S20. Correlation between the cumulative carbon leakage and the alkalinity change of the first river segment (relative to its concurrent background state) of each flow path over duration of 1 day. The correlation coefficient (r) and the p-value are also shown.

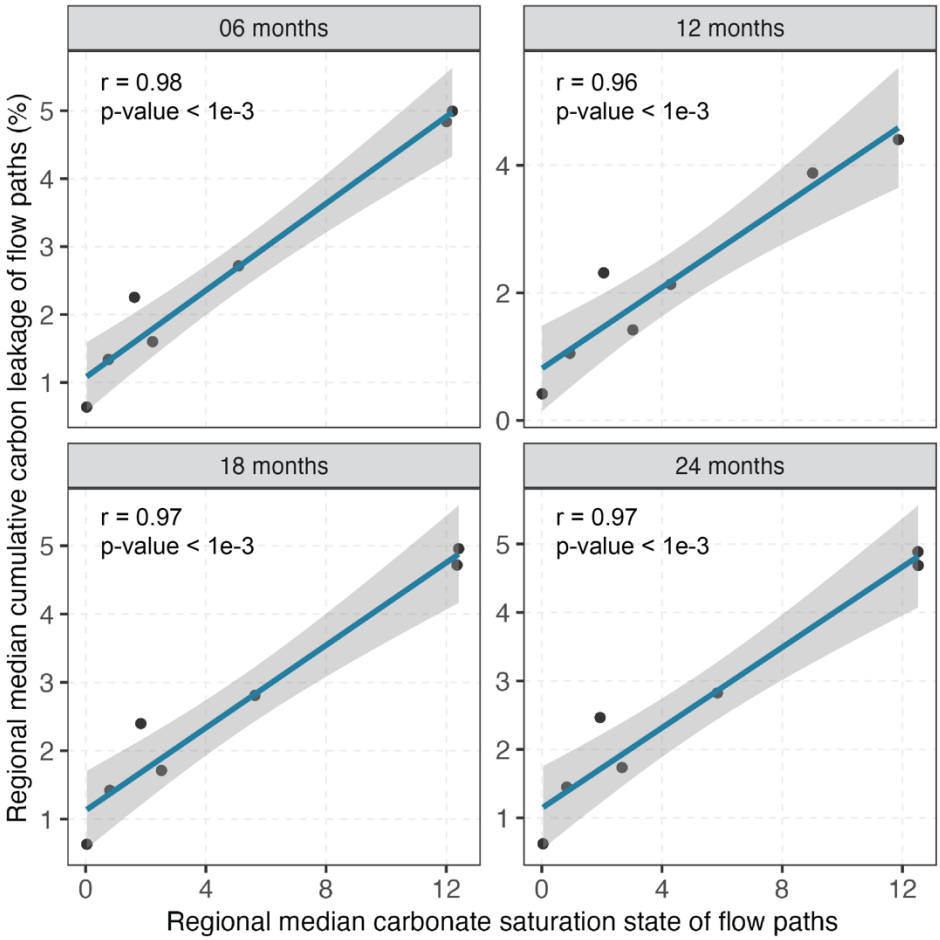

Figure S21. Correlation between the regional median carbonate saturation state and the regional median cumulative carbon leakage rate over durations of 6, 12, 18, and 24 months. The correlation coefficient (r) and the p-value are also shown.